Variational multiscale turbulence modelling in a high order spectral element method

Carl Erik Wasberg *, Thor Gjesdal, Bjørn Anders Pettersson Reif, Øyvind Andreassen

Norwegian Defence Research Establishment (FFI), P.O. Box 25, NO-2027 Kjeller, Norway

ABSTRACT

In the variational multiscale (VMS) approach to large eddy simulation (LES), the governing equations are projected onto an a priori scale partitioning of the solution space. This gives an alternative framework for designing and analyzing turbulence models. We describe the implementation of the VMS LES methodology in a high order spectral element method with a nodal basis, and discuss the properties of the proposed scale partitioning. The spectral element code is first validated by doing a direct numerical simulation of fully developed plane channel flow. The performance of the turbulence model is then assessed by several coarse grid simulations of channel flow at different Reynolds numbers.

© 2009 Elsevier Inc. All rights reserved.

1. Introduction

Large eddy simulations (LES) provides a physically appealing framework for turbulent flow prediction, where the three-dimensional and time-dependent motion of the largest turbulent scales are solved directly, with complete time and space resolution. These scales are in general associated with the most energetic motion of the turbulence field and it is ideally only the least energetic motion that need to be modelled. The concept is therefore well suited to confront the scale complexity and transient behaviour inherent to turbulent flows.

In traditional LES, large- and small-scale motion are separated by applying a spatial filtering operation to the Navier–Stokes equations before discretization. Hence, there are two layers of approximation, filtering and truncation, that both contribute to the modelling error. Filtering may be explicitly carried out, or only implicitly assumed. The result is a set of equations for the large-scale motion. The residual motion, i.e. motions on scales that are smaller than the filter width, appear in these equations as a residual stress term. This term is a priori unknown, and although the intention is not to describe the residual motion in itself, the term must be modelled to incorporate the effect of the residual motion on the resolved scales.

There are several conceptual issues in filter-based LES that have to be addressed. For instance, filtering and spatial differentiation do not in general commute on bounded domains or for non-uniform grids, so careful analysis is needed to obtain the correct form of the equations. It is also not obvious how to prescribe correct boundary conditions for the filtered velocity

---

at solid walls. Another unwarranted character of filter-based LES models is that the residual stress model may adversely affect the resolved part of the energy spectrum. These issues have been the subject of a considerable amount of research. For example have Carati et al. [1] analysed the error contributions from the two layers of approximation – filtering and truncation. They show that the filtering error can be expressed in terms of the resolved velocity field and that the purpose of the subgrid model is to account for the effect of the unresolved motion, i.e. the truncation errors. In general, the lesson learned is that LES works well in cases where the rate-controlling dynamical processes occur at the largest (resolved) scales of motion, or equivalently in flows where the unresolved scales, and consequently the model, only plays a secondary dynamical role.

In this paper we consider a different approach to LES, the variational multiscale (VMS) LES method originally proposed by Hughes et al. [2]. This formulation is based on a variational (or weak) form of the Navier–Stokes equations in unfiltered form. Consequently, there is no filtering error and it is evident that the role of the model term is to compensate for the truncation errors, fully in line with the analysis in [1]. The VMS LES method employs a scale partitioning of the solution space, and variational projection of the Navier–Stokes equations onto the different scale ranges. Since the scale partitioning operators do not act on the governing equations, the same way as a filter does, commutation between scale partitioning and differentiation is not an issue. The projected equations, given in Section 2, contain all the terms that represent interaction between the scales, and are therefore a well suited tool for clarifying assumptions and prescribing models for the LES. In addition, one of the scale partitioning operators are chosen to coincide with the discretization.

The scale partitioning used in this paper divides the solution space into three subspaces, the large resolved scales, the small resolved scales, and the unresolved scales. The definition of resolved scales in this context is the spatial scales that can be represented by the numerical discretization. The scale partitioning is sketched in Fig. 1. In this figure, as well as in the rest of this paper, "small" scales refer the subspace consisting of small *resolved* scales, even though the scales are not necessarily physically small when the resolution is coarse.

We implement the resulting VMS LES formulation in a spectral element method for the solution of the Navier–Stokes equations. Spectral element methods are related to both spectral methods and finite element methods, and combine high order accuracy with geometric flexibility. These properties makes it attractive to develop good turbulence models for the spectral element method, because the potential for providing good LES results in more realistic cases, including more complex geometries, is there if the right model is found. Another important point is that the high order accuracy provides us with an attractive framework for model development in which the numerical errors can be controlled, such that the true performance of the model can be assessed. In this paper we focus on the simple geometry of plane channel flow, a much used example in turbulence modelling with good reference solutions available.

The first implementations of the variational multiscale LES method [3–5] used global spectral methods. These methods naturally employ an orthogonal modal basis, such that the scale partitioning becomes straightforward. The method has also been implemented in the context of other numerical schemes, such as finite element methods [6–8] and finite volume methods [9]. The potential of the VMS methodology has been demonstrated by several numerical studies, for various flow configurations, in which different VMS implementations have been shown to perform comparable or better than the classical dynamic Smagorinsky procedure [3–5,10,11]

Our spectral element code uses an element-wise discretization with nodal basis functions that contain information on all the scales. The partitioning into large and small scales is done through the use of an element-by-element transformation into the Legendre modal basis functions, rather than by using a global spectrum.

In the following sections we will discuss the variational multiscale method as a turbulence modelling tool, and describe the spectral element implementation of the method. Finally we will present computed results from both a high-resolution direct numerical simulation (DNS) and coarse grid VMS LES for fully developed turbulent flow in a plane channel at frictional Reynolds numbers $Re_\tau = 180, 550$, and 950. The latter case represents, to our knowledge, the highest Reynolds number that has been reported in a VMS LES setting. The computed results show that, even with simple modelling applied to the small-scale equations, the performance of the methodology is promising.
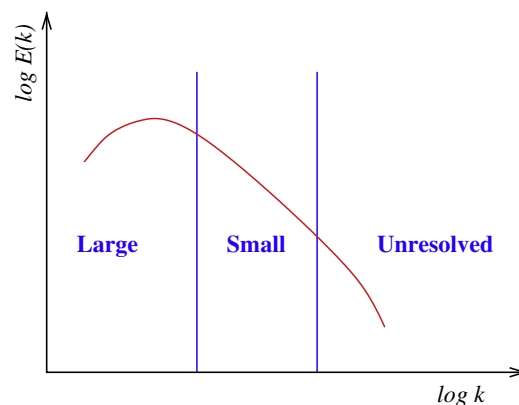

Fig. 1. Schematic of the turbulent energy spectrum as a function of wavenumber, with scale partitioning.

2. The variational multiscale method

The variational multiscale LES method was introduced by Hughes et al. [2] and later elaborated by Collis [12]. We will outline the method following Collis, to shed light on the modelling assumptions employed in the derivation of the model.

The Navier–Stokes equations describing the dynamics of a viscous, incompressible fluid are

$$\frac{\partial \boldsymbol{u}}{\partial t} + \boldsymbol{u} \cdot \nabla \boldsymbol{u} = -\frac{1}{\rho}\nabla p + v\nabla^2 \boldsymbol{u} + \boldsymbol{f}, \tag{1a}$$

$$\nabla \cdot \boldsymbol{u} = 0, \tag{1b}$$

where the independent variables are the velocity, $\boldsymbol{u} = (u, v, w)$, and the pressure, p. The kinematic viscosity is denoted by v, and $\boldsymbol{f}$ is a body force term. For ease of presentation of the variational multiscale method we assume homogeneous Dirichlet boundary conditions for the velocity.

We can construct the weak, or variational, formulation by choosing test and trial functions in the same function space $\mathcal{V}$. Note however that in general the test and trial spaces will differ at the boundary because we require the test functions to vanish there, while $\boldsymbol{u}$ may not. Let

$$U = (\boldsymbol{u}, p) \in \mathcal{V}, \quad W = (\boldsymbol{w}, q) \in \mathcal{V}, \quad F = (\boldsymbol{f}, 0).$$

We take the inner product of W with Eq. (1b) (written in the compact form $\mathcal{N}(U) = F$) to obtain the weak Navier–Stokes operator:

$$\langle W, \mathcal{N}(U)\rangle \equiv \mathcal{L}(W, U) - \mathcal{R}(\boldsymbol{w}, \boldsymbol{u}) = \langle W, F\rangle, \tag{2}$$

comprising the bi-linear Stokes operator

$$\mathcal{L}(W, U) \equiv \left\langle \boldsymbol{w}, \frac{\partial \boldsymbol{u}}{\partial t}\right\rangle - \langle \nabla \cdot \boldsymbol{w}, p\rangle + \langle \nabla^s \boldsymbol{w}, 2v\nabla^s \boldsymbol{u}\rangle + \langle q, \nabla \cdot \boldsymbol{u}\rangle, \tag{3}$$

and non-linear advection represented by the Reynolds projection

$$\mathcal{R}(\boldsymbol{w}, \boldsymbol{u}) = \mathcal{B}(\boldsymbol{w}, \boldsymbol{u}, \boldsymbol{u}). \tag{4}$$

The components of the symmetric rate of strain are defined as

$$(\nabla^s \boldsymbol{u})_{ij} = \frac{1}{2}\left(\frac{\partial u_i}{\partial x_j} + \frac{\partial u_j}{\partial x_i}\right), \tag{5}$$

and $\mathcal{B}$ is the tri-linear term

$$\mathcal{B}(\boldsymbol{w}, \boldsymbol{u}, \boldsymbol{v}) \equiv \langle \nabla \boldsymbol{w}, \boldsymbol{u}\boldsymbol{v}\rangle. \tag{6}$$

To take into account the multiscale representation, we write the solution space $\mathcal{V}$ as a disjoint sum

$$\mathcal{V} = \overline{\mathcal{V}} \oplus \widetilde{\mathcal{V}} \oplus \widehat{\mathcal{V}},$$

in which $\overline{\mathcal{V}}$ and $\widetilde{\mathcal{V}}$ comprise the large and small resolved scales, respectively, whereas $\widehat{\mathcal{V}}$ contains the unresolved scales.

Decomposing the test and trial functions in these spaces gives

$$U = \overline{U} + \widetilde{U} + \widehat{U}, \quad W = \overline{W} + \widetilde{W} + \widehat{W},$$

and we can develop a set of scale-projected equations from the projections

$$\langle \overline{W}, \mathcal{N}(U)\rangle = \langle \overline{W}, F\rangle, \quad \langle \widetilde{W}, \mathcal{N}(U)\rangle = \langle \widetilde{W}, F\rangle, \quad \langle \widehat{W}, \mathcal{N}(U)\rangle = \langle \widehat{W}, F\rangle. \tag{7}$$

Using (3)–(6) and introducing the cross stress term

$$\mathcal{C}(\boldsymbol{w}, \boldsymbol{u}, \boldsymbol{u}') = \mathcal{B}(\boldsymbol{w}, \boldsymbol{u}, \boldsymbol{u}') + \mathcal{B}(\boldsymbol{w}, \boldsymbol{u}', \boldsymbol{u}), \tag{8}$$

(7) can be written out as

$$\mathcal{L}(\overline{W}, \overline{U}) + \mathcal{L}(\overline{W}, \widetilde{U}) - \mathcal{R}(\bar{\boldsymbol{w}}, \bar{\boldsymbol{u}}) - \langle \overline{W}, F\rangle - \mathcal{R}(\bar{\boldsymbol{w}}, \tilde{\boldsymbol{u}}) - \mathcal{C}(\bar{\boldsymbol{w}}, \bar{\boldsymbol{u}}, \tilde{\boldsymbol{u}})$$
$$= -\mathcal{L}(\overline{W}, \widehat{U}) + \mathcal{R}(\bar{\boldsymbol{w}}, \hat{\boldsymbol{u}}) + \mathcal{C}(\bar{\boldsymbol{w}}, \bar{\boldsymbol{u}}, \hat{\boldsymbol{u}}) + \mathcal{C}(\bar{\boldsymbol{w}}, \tilde{\boldsymbol{u}}, \hat{\boldsymbol{u}}), \tag{9a}$$

$$\mathcal{L}(\widetilde{W}, \widetilde{U}) + \mathcal{L}(\widetilde{W}, \overline{U}) - \mathcal{R}(\tilde{\boldsymbol{u}}, \tilde{\boldsymbol{u}}) - \langle \widetilde{W}, F\rangle - \mathcal{R}(\tilde{\boldsymbol{u}}, \bar{\boldsymbol{u}}) - \mathcal{C}(\tilde{\boldsymbol{u}}, \bar{\boldsymbol{u}}, \tilde{\boldsymbol{u}})$$
$$= -\mathcal{L}(\widetilde{W}, \widehat{U}) + \mathcal{R}(\tilde{\boldsymbol{w}}, \hat{\boldsymbol{u}}) + \mathcal{C}(\tilde{\boldsymbol{u}}, \bar{\boldsymbol{u}}, \hat{\boldsymbol{u}}) + \mathcal{C}(\tilde{\boldsymbol{w}}, \tilde{\boldsymbol{u}}, \hat{\boldsymbol{u}}), \tag{9b}$$

$$\mathcal{L}(\widehat{W}, \widehat{U}) + \mathcal{L}(\widehat{W}, \overline{U}) + \mathcal{L}(\widehat{W}, \widetilde{U}) - \mathcal{R}(\hat{\boldsymbol{w}}, \hat{u}) - \mathcal{C}(\hat{\boldsymbol{w}}, \bar{\boldsymbol{u}}, \hat{\boldsymbol{u}}) - \mathcal{C}(\hat{\boldsymbol{w}}, \tilde{\boldsymbol{u}}, \hat{\boldsymbol{u}})$$
$$= \mathcal{R}(\hat{\boldsymbol{w}}, \bar{\boldsymbol{u}}) + \mathcal{R}(\hat{\boldsymbol{w}}, \tilde{\boldsymbol{u}}) + \mathcal{C}(\hat{\boldsymbol{w}}, \bar{\boldsymbol{u}}, \tilde{\boldsymbol{u}}) + \langle \widehat{W}, F\rangle. \tag{9c}$$

We have written the first two of these equations in a form such that all terms that depend on the unresolved scales are collected in the right-hand sides. It is thus evident that there is an effect of the unresolved scales on the resolved scales. In the original paper by Hughes et al. [2], the modelling assumptions were not stated, but the issue was clarified by Collis [12], who showed that essentially the following assumptions result in a method that is identical to the method proposed by Hughes:

- The separation in wavenumber space between large and unresolved scales is sufficiently large so that there is negligible *direct* dynamic influence from the unresolved scales on the large scales.
- The dynamic impact of the unresolved scales on the small scales is on average dissipative in nature.

The consequence of the first assumption is that the right-hand side of (9a) is set to zero, while the effect of the second assumption is to replace the right-hand side of (9b) with a dissipative model term. The simple Smagorinsky-type model is in an averaged sense fully consistent with the second assumption. In order to approximate the temporal behaviour at the cut-off, a more refined modelling approach would be needed. This is however outside the scope of the present study.

With these assumptions, the LES model is only applied to the small-scale projection equation. Different implementations of this method by Hughes and coworkers [3,4], by Ramakrishnan and Collis [5], and by Jeanmart and Winckelmans [13,14] have produced encouraging results for simple model problems.

Our objective is to present an implementation of the VMS LES formulation in the spectral element method, so we consider it outside the scope of the present paper to discuss alternatives to the two assumptions given above. We merely note in passing that the variational multiscale methodology provides a framework well suited for more sophisticated model formulation.

Bearing the above in mind, we can formulate the variational modelled equations. The projection onto the unresolved scales is naturally omitted, and the resulting set of equations is

$$\mathcal{L}(\overline{W},\overline{U}) + \mathcal{L}(\overline{W},\widetilde{U}) - \mathcal{R}(\overline{\boldsymbol{w}},\overline{\boldsymbol{u}}) - \mathcal{R}(\overline{\boldsymbol{w}},\tilde{\boldsymbol{u}}) - \mathcal{C}(\overline{\boldsymbol{w}},\overline{\boldsymbol{u}},\tilde{\boldsymbol{u}}) - \langle\overline{W},F\rangle = 0, \tag{10a}$$

$$\mathcal{L}(\widetilde{W},\widetilde{U}) + \mathcal{L}(\widetilde{W},\overline{U}) - \mathcal{R}(\tilde{\boldsymbol{w}},\overline{\boldsymbol{u}}) - \mathcal{R}(\tilde{\boldsymbol{w}},\tilde{\boldsymbol{u}}) - \mathcal{C}(\tilde{\boldsymbol{w}},\overline{\boldsymbol{u}},\tilde{\boldsymbol{u}}) - \langle\widetilde{W},F\rangle = -\langle\nabla^s\tilde{\boldsymbol{w}}, 2\nu_T\nabla^s\tilde{\boldsymbol{u}}\rangle. \tag{10b}$$

The terms that couple the different scales are evident in (10b); all the original terms coupling the large and small resolved scales are retained, whereas the small-scale projection equation has been supplemented with a dissipative term on the right-hand side that accounts for the interactions between the small and the unresolved scales.

We are, however, chiefly concerned with the complete resolved solution $\widetilde{U} = \overline{U} + \widetilde{U}$, not with the large and small scales per se. Adding the large- and small-scale projections we obtain

$$\left\langle\overline{\widetilde{W}},\mathcal{N}(\overline{\widetilde{U}})\right\rangle + \langle\nabla^s\tilde{\boldsymbol{w}}, 2\nu_T\nabla^s\tilde{\boldsymbol{u}}\rangle = \langle\overline{\widetilde{W}},F\rangle. \tag{11}$$

We note that in this equation, all the interaction terms between the large and the small scales are accounted for in the advection operator $\mathcal{R}$, which is part of the first term on the left-hand side in (11). The projected cross and Reynolds stress terms that appear in the large- and small-scale Eq. (10b) can be useful for analysis and turbulence modelling, but do not necessarily impact on the implementation of the method. The variational formulation is hence primarily used as a framework for clarifying the modelling assumptions and selecting appropriate model terms. The essential feature of the method is that the turbulence modelling should be confined to the small scales. As long as a suitable scale partitioning can be performed on the solution space, the methodology can in principle be applied to any discretization, as indicated by Hughes et al. [3].

2.1. Some related methods

There are other methods that share some of the elements of the present VMS LES method. One method is the spectral vanishing viscosity (SVV) method, first introduced for hyperbolic conservation laws by Tadmor [15]. For comparison with VMS LES, we use the spectral element formulation by Xu and Pasquetti [16] and restrict the discussion to the one-dimensional case without coordinate scaling, to avoid technicalities. The SVV term of [16] is given in the form

$$\varepsilon_N \left\langle Q^{1/2}(\partial_x u_N), Q^{1/2}(\partial_x v_N)\right\rangle_{L^2(\Lambda)},$$

where Q is an operator that selects only the modes with high wave numbers – with a smooth spectral representation from zero on low wave numbers to one on high wave numbers. If we view $Q^{1/2}$ as a small-scale extraction operator (albeit different from the one used in this paper), we can write the term $Q^{1/2}(\partial_x u_N)$ as $\widetilde{\nabla\boldsymbol{u}}$, and the SVV method as

$$\left\langle\overline{\widetilde{W}},\mathcal{N}(\overline{\widetilde{U}})\right\rangle + \varepsilon_N\langle\widetilde{\nabla w},\widetilde{\nabla u}\rangle = \langle\overline{\widetilde{W}},F\rangle \tag{12}$$

in the notation of this paper. There are four main differences between (12) and the present VMS LES method, namely the reversed sequence of the (non-commuting) scale extraction and differentiation operator; the use of the symmetric gradient (5); the form of the small-scale extraction operator (defined in Section 3.2); and the difference between $\varepsilon_N = O(1/N)$ and ν_T. The particular form of ν_T is discussed in Section 3.5, we just note here that it contains a $1/N^2$-factor (through the term Δ'^2) and a velocity gradient, which makes it vary through the domain. However, it should be noted that apart from the sequence

of the operators, the SVV method in the form (12) could have been formulated within the VMS LES formalism. The principle of basing the scale-dependent operators on the local Legendre modal representation on each element is also common to both methods.

Vreman [17] describes a filter-based LES method that is analogous to VMS LES in the sense that the modelled subgrid term is filtered twice to only contain "small-scale resolved" contributions. Another method, which does not involve interchanging filtering and differentiation operators, is also described by Vreman in the same paper. The comparison of the two methods illustrates the differences and similarities between VMS and "traditional" LES.

Jeanmart and Winckelmans [13,14] use essentially the same approach as Vreman to develop the "Regularized Variational Multiscale Model". In this method, a smooth discrete high-pass filter is employed to extract the small scales and to compute the VMS model term, which is evaluated explicitly. Note that by using a smooth filter, the large and small function spaces are no longer necessarily disjoint as in the original derivation of the VMS method.

3. Incorporation of VMS LES in the spectral element method

In this section we describe the implementation of a VMS LES model in a high order spectral element method for the solution of the incompressible Navier–Stokes equations. More basic details about the spectral element method can be found in [18,19].

3.1. Spectral element Navier–Stokes solver

To solve the Navier–Stokes Eq. (1b) we employ an implicit-explicit time splitting in which we integrate the advective term explicitly, while the diffusive term, the pressure term, and the divergence equation are treated implicitly. After discretization in time we can write (1b) in the form

$$(\alpha I - v\nabla^2)\boldsymbol{u}^{n+1} = -\nabla p^{n+1} + \boldsymbol{g}(\boldsymbol{f}^{n+1}, \boldsymbol{u}^n, \boldsymbol{u}^{n-1}, \ldots),$$ (13a)

$$\nabla \cdot \boldsymbol{u}^{n+1} = 0,$$ (13b)

in which the explicit treatment of the advection term is included in the source term $\boldsymbol{g}$. In the actual implementation we use the second order (in time) accurate formula BDF2, which gives $\alpha = 3/2\Delta t$ in (13b), while we compute the advective contributions according to the operator-integration-factor (OIF) method [20].

The spatial discretization is done with a spectral element method [21,22], where the weak formulation of (13b) is solved on a set of non-overlapping hexahedral elements. Within each element, trial and test functions are constructed as tensor products of Lagrangian interpolants of Legendre polynomials. The integrals in the weak formulation are calculated by the Gauss–Lobatto–Legendre (GLL) or Gauss–Legendre (GL) integration formulas, which can be viewed as discrete inner products. To avoid spurious pressure modes, the polynomial order of the pressure representation is taken to be two orders lower than for the velocity components (the "$\mathbb{P}_N - \mathbb{P}_{N-2}$" method [22]).

The discrete inner products are consistent with the approximation error (Section 9.3 [23]) for the linear terms of (13b). However, the explicitly treated advection sub-problem contains non-linear terms, which are a potential source of aliasing errors. If not controlled, such errors may be detrimental to the stability of the method. The most fundamental approach to de-aliasing is to perform over-integration [24] – that is, to over-sample by a factor 3/2 and calculate the quadrature at this refined grid for the inner products containing non-linear terms. This ensures that the numerical quadrature error from the integration of the non-linear term is consistent with the other quadrature errors in the method. The errors corrected by over-integration can represent both positive and negative energy, so over-integration is not a dissipative mechanism. However, it is the positive energy errors that are potentially damaging for a marginally resolved calculation.

The overhead involved depends on the amount of the total computational time that is originally spent on the advection part, but for the calculations presented here, over-integration typically leads to an increase of around 20% of computational time.

An alternative, and computationally more efficient approach, is to use polynomial filtering of the solutions as proposed by Fischer and Mullen [25], where a simple filter operator with negligible computational cost is applied to the solution at every time-step. The effect in the spectral space on each element is to transfer a certain fraction (the filter strength) of the energy on the highest order basis polynomial in each element over to the third-highest order polynomial [26]. By this operation, the pile-up of energy on the highest order polynomial is reduced, while the values at the element boundaries are unchanged. Filter strengths as small as 1–5% can have positive effects on the solution. As for over-integration, this is not a dissipative mechanism, as it can either increase or decrease the energy [26]. The stabilizing effect is not as strong as for over-integration, but the method is attractive because of its simplicity. If desirable, the methods can be used in combination.

For the solution of the discrete system of equations we use the global three-dimensional stiffness, mass, and differentiation matrices, A, B, and D (see [18,19] for definitions), to define discrete operators for the full system:

$$\mathcal{A} = \text{diag}(A, A, A), \quad \mathcal{B} = \text{diag}(B, B, B), \quad \mathcal{D} = (D_x, D_y, D_z),$$ (14)

and the discrete Helmholtz operator $\mathcal{H} = \alpha\mathcal{B} + v\mathcal{A}$. Appropriate boundary conditions should be included in these discrete operators. This gives the discrete equations

$$\mathcal{H}u^{n+1} - \mathcal{D}^T p^{n+1} = \mathcal{B}f^{n+1}, \tag{15a}$$

$$-\mathcal{D}u^{n+1} = 0, \tag{15b}$$

where the change of sign in the pressure gradient term is caused by an integration by parts in the construction of the weak form of the problem. Note that vectors of discrete point values are not written in bold, and that u in (15) represents the combined vector of point values for all three velocity components.

This discrete system is solved efficiently by a pressure correction method, second order accurate in time (Section 6.2.3 [18]):

$$\mathcal{H}u^* = \mathcal{B}f^{n+1} + \mathcal{D}^T p^n, \tag{16a}$$

$$\mathcal{D}\mathcal{B}^{-1}\mathcal{D}^T(p^{n+1} - p^n) = -\alpha \mathcal{D}u^* \tag{16b}$$

$$u^{n+1} = u^* + \frac{1}{\alpha}\mathcal{B}^{-1}\mathcal{D}^T(p^{n+1} - p^n), \tag{16c}$$

where u^* is an auxiliary velocity field that does not satisfy the continuity equation, i.e. $\mathcal{D}u^* \neq 0$.

The discrete Helmholtz operator is symmetric and diagonally dominant, since the mass matrix of the Legendre discretization is diagonal, and can be efficiently solved by the conjugate gradient method with a diagonal (Jacobi) preconditioner. Whereas the pressure operator $\mathcal{D}\mathcal{B}^{-1}\mathcal{D}^T$ is easily computed; it is ill-conditioned. The pressure system is solved by the preconditioned conjugate gradient method, with a multilevel overlapping Schwarz preconditioner based on linear finite elements [27].

3.2. Discrete scale partitioning operators

The implementations of the variational multiscale LES method reported in [3–5] used global spectral methods. These methods naturally employ an orthogonal modal basis, such that the scale partitioning becomes straightforward. Our spectral element code uses a discretization based on the Legendre polynomials, which offer an orthogonal hierarchical basis on each element.

The *modal* representation of a one-dimensional function $w(x)$ on a single element is

$$w_h(x) = \sum_{j=0}^{N-1} c_j \sqrt{\frac{2j+1}{2}} L_j(x), \quad -1 \leqslant x \leqslant 1, \tag{17}$$

where $L_j(x)$ is the jth order Legendre polynomial, and c_j are the spectral coefficients. The factor $\sqrt{\frac{2j+1}{2}}$ is used to normalize the basis. The scaled Legendre polynomials represents a natural orthonormal basis, in which it is straightforward to perform the scale partitioning. In this setting, it is natural to associate the low order polynomials with the large scales and the higher order polynomials with the smaller scales.

Like the majority of the spectral element community, we do however use a *nodal* basis constructed from the Lagrangian interpolant functions. In this case all the basis functions contain information on all Legendre modes, so the transformation to the modal basis is needed:

$$Kc = w, \quad K_{ij} = \sqrt{\frac{2j+1}{2}} L_j(\xi_i), \tag{18}$$

where c is the vector of spectral coefficients and w is the vector of function values at the GLL grid points $\{\xi_j\}_{j=0}^{N-1}$. Note that the scale partitioning operators need only to be defined for the GLL (velocity) grid, since the small-scale pressure does not appear in (11).

Let $N = \overline{N} + \widetilde{N}$, such that $\overline{N}$ is the dimension of the polynomial basis for the large scales and $\widetilde{N}$ is the dimension of the small-scale space. The large-scale part of w can then be written as

$$\overline{w} = KTK^{-1}w, \tag{19}$$

where $T = \mathrm{diag}(I_{\overline{N}}, 0_{\widetilde{N}})$ is the operator that annihilates the small-scale components in the modal basis. For notational convenience, we define the large-scale extraction operator

$$L = KTK^{-1},$$

while the corresponding small-scale extraction operator is

$$S = I - L.$$

When tensor products of these operators are formed in higher dimensions, the resulting operators extract the components with large-scale, or small-scale, respectively, components in *all* dimensions. The sum of these two operators does not add up to the identity, so we choose to define the three-dimensional small-scale extraction operator to be

$$S = I - (L_z \otimes L_y \otimes L_x). \tag{20}$$

This is illustrated in two dimensions in Fig. 2. The resulting small-scale extraction operator returns functions with small-scale structure in *at least one* dimension.

For multiple elements, the operators defined above are applied element-wise. This means that there is no *global* scale extraction other than the sum of the extractions from each element. The result is that e.g. the small-scale extraction $\bar{\bar{u}}$ in (11) is discontinuous across element interfaces, and so are its derivatives. This is not unusual in spectral element methods, in fact both the pressure (because of the "staggered" GL grid) and all derivatives of velocity and pressure share this property. In the weak formulation, continuity of the velocity field is ensured through the "direct stiffness summation" over all elements, which calculates weighted averages of all terms at the element interfaces [18,19].

3.3. Properties of the large-small partition

As described above, the large-scale extraction operator corresponds to a sharp cut-off in the element-wise Legendre modal space. In this section we shall illustrate the effect in the global Fourier space of this partitioning and discuss the relation between element-wise Legendre modes and global Fourier modes.

We start by considering the highest Fourier wave numbers that can be represented on a given spectral element grid. A minimum of π polynomials per wavelength are required for rapid convergence of the Legendre expansion of a Fourier component [28]. Consequently, on a spectral element grid on $[0, 2\pi\rangle$ with M elements and N grid points on each element, higher wave numbers than approximately NM/π can not be accurately represented.

Fig. 3 shows the local Legendre spectra of the first 8 global Fourier modes using $M = 4$ elements with $N = 7$ polynomials on each element. More precisely, the coefficients c_j in the modal representation (17) are calculated for the functions $e^{ik\pi x/4}$ with $k = 0, \ldots, 7$. Except the first mode, which is constant in both the Fourier and Legendre bases, each Fourier mode is represented by the full set of Legendre modes. The lowest Fourier modes have rapidly decaying Legendre spectra, which means they will mainly be represented by the large-scale partition. However, the higher Fourier modes have significant contributions also from the lower Legendre modes, and they will consequently be split between the large- and small-scale partitions. An important result is that the large-scale partition will be more dominant than for a corresponding sharp cut-off in the Fourier space.

To further illustrate the properties of the large-small partitioning, we consider a "full" cosine spectrum, consisting of all the well representable wave numbers,

$$f(x) = \sum_{k=0}^{K_{\max}} \cos(kx). \tag{21}$$

The large-small partitioning by sharp cutoffs in the local Legendre expansions is applied using $\overline{N} = 4$ of the 7 modes (57%) on each element as the large-scale space. The resulting large- and small-scale functions are globally sampled on a 128-point regular grid and represented as cosine series. The results are given in Fig. 4 for two SEM grids on $[0, 2\pi\rangle$ with $N = 7$ in both cases, $M = 4$ and $K_{\max} = 8$ to the left, and $M = 10$ and $K_{\max} = 20$ to the right. These grids have the same number of elements and grid points as the "Coarse-24" and "Coarse-60" grids used in the VMS LES calculations reported in Sections 4.4 and 4.6. The "full scale" coefficients in Fig. 4 represent the sum of the partitions, and illustrates how well the function (21) is approximated on each spectral element grid.

An important point illustrated by Fig. 4 is that although the scale partitioning in the Legendre space is done as a sharp cut-off, the Fourier spectra of the two partitions are relatively smooth. The reason for this is that each of the original cosine terms is represented by a combination of local Legendre modes on each element. It has been argued that a smooth spectral partitioning is preferable. Sagaut and Levasseur [29] performed simulations of decaying isotropic turbulence and showed that a smooth small-scale extraction operator reduces unphysical energy pile-up at the small scales. Meyers and Sagaut [30]
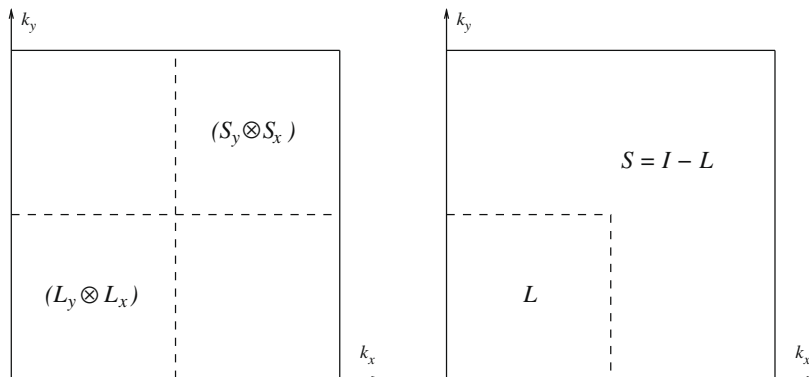

Fig. 2. Large- and small-scale partitions in the 2-dimensional polynomial wavenumber space. The chosen partition operators are shown to the right.
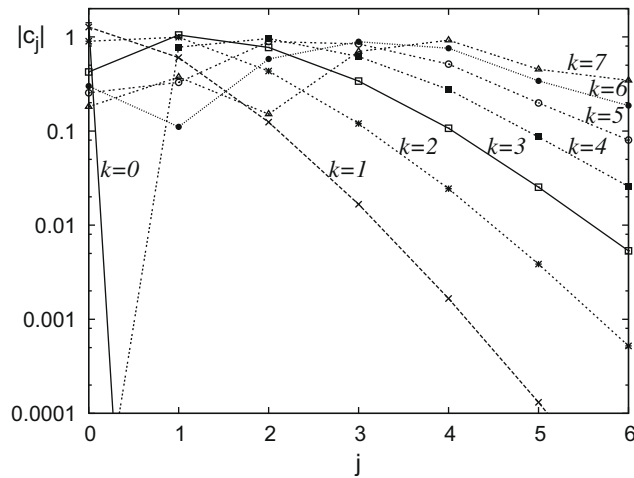
Fig. 3. Local Legendre spectra of global Fourier modes.
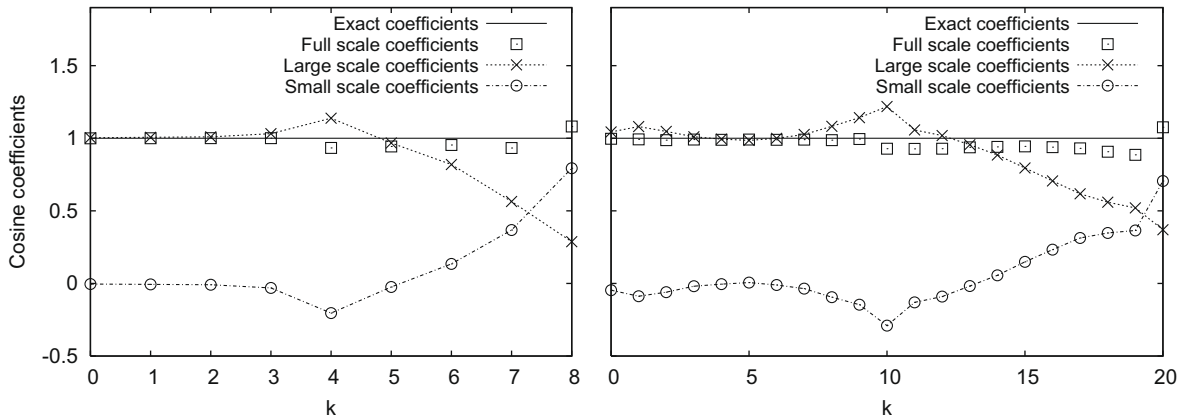

Fig. 4. Cosine series representations of a sharp cut-off in Legendre modal space. Left: 4 elements and maximum wavenumber 8; Right: 10 elements and maximum wavenumber 20. Seven grid points per element in both cases, with 4 Legendre modes in the large-scale partition.

analyzed the dissipation properties of both traditional and Variational Multiscale Smagorinsky models, and showed that smooth small-scale extraction operators lead to more physically robust VMS models.

The spectra of the large- and small-scale partitions are very similar on the two grids used in Fig. 4, and the gradual growth in the small-scale spectrum starts around the cut-off percentage (57%), again showing that the impact of the small-scale extraction is weaker when the sharp cut-off is applied to the local Legendre expansions. An effect of increasing the number of elements is that more Fourier components can be represented, and the cut-off point for the large-small partitioning corresponds to a higher Fourier wavenumber. This could represent a problem if the cut-off frequency had a physical meaning, but the terms "large" and "small" scales are only relative to the given resolution of a simulation, and hence it is meaningful to designate fixed fractions of the local Legendre spectra to the two partitions.

In the same vein it can be discussed whether the cut-off point in the local Legendre space should vary in a more general case with variable element sizes. A guideline for this could be to make the Fourier wavenumber corresponding to the Legendre cut-off approximately constant throughout the whole domain. In the channel simulations described in Section 4 this situation occurs, as the elements are smaller in the wall-normal direction closer to the wall. We take the point-of-view that the same fraction of the local Legendre spectrum should be used for partitioning for all elements, arguing as above about the relativity of the large and small scales. If the cut-off point was changed to a lower order Legendre polynomial for a smaller element close to a wall in order to maintain the same "physical" cut-off scale, the effect of refining the element grid would be reduced.

3.4. Implementation of the model term

We now turn our attention to the implementation of the variational multiscale model term $\langle \nabla^s \tilde{\boldsymbol{w}}, 2\nu_T \nabla^s \tilde{\boldsymbol{u}} \rangle$ from (11). Note that the turbulent eddy viscosity ν_T is not a material property of the fluid, but a property of the flow field and as such varies through the flow domain.
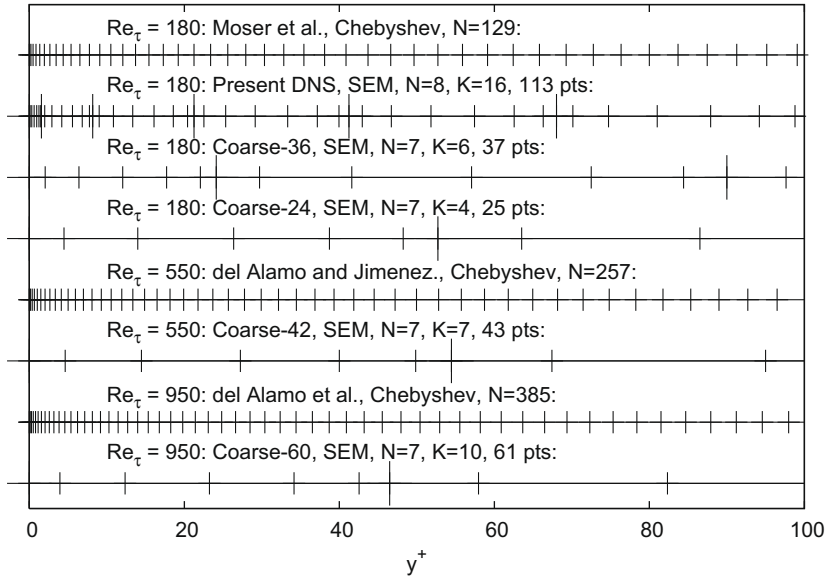
Fig. 5. Details of the point and element distribution in the wall-normal direction for the grids listed in Tables 1 and 2. The longer bars show element interfaces for the spectral element grids.

It is instructive to first consider the one-dimensional case with a constant eddy viscosity. Furthermore, for ease of exposition, we only consider a single element. In this case, the model term above is

$$\nu_T \int_\Omega \frac{\partial \tilde{w}}{\partial x} \frac{\partial \tilde{u}}{\partial x} \, dx, \quad x \in \Omega. \tag{22}$$

The Lagrangian interpolants used as test- and trial functions are denoted $h_i(x)$, where $h_i(\xi_j) = \delta_{ij}$ when ξ_j is a quadrature grid point. A function $v(x)$ is then represented by the interpolating polynomial

$$v_h(x) = \sum_{i=0}^{N-1} v_i h_i(x), \quad v_i = v(\xi_i). \tag{23}$$

Using the small-scale extraction operator defined above, we have

$$\tilde{u}(x) = \sum_{m=0}^{N-1} \sum_{q=0}^{N-1} S_{mq} u_q h_m(x), \tag{24}$$

and for a given test function on Lagrange form ($w^i(x) = h_i(x)$)

$$\tilde{w}^i(x) = \sum_{p=0}^{N-1} S_{pi} h_p(x). \tag{25}$$

Inserting these representations and using the discrete inner product based on Gauss–Lobatto quadrature, we obtain

$$\langle \nabla \tilde{w}^i, \nabla \tilde{u} \rangle_h = \sum_{r=0}^{N-1} \sum_{p=0}^{N-1} \sum_{m=0}^{N-1} \sum_{q=0}^{N-1} S_{pi} h'_p(\xi_r) S_{mq} u_q h'_m(\xi_r) \rho_r = \sum_{p=0}^{N-1} S_{pi} \sum_{m=0}^{N-1} \sum_{q=0}^{N-1} S_{mq} u_q A^x_{pm} = \sum_{q=0}^{N-1} (S^T A^x S)_{iq} u_q = (S^T A^x S u)_i$$
$$= ((I-L)^T A^x \tilde{u})_i, \tag{26}$$

where A^x is the one-dimensional stiffness matrix. Inserting a single test function, as in (26), gives one row of the operator acting on u, while using the whole set of test functions defines a discrete operator:

$$\langle \nabla \tilde{w}, \nabla \tilde{u} \rangle_h \leftrightarrow (I-L)^T A^x \tilde{u}. \tag{27}$$

It is easily seen from the penultimate line of (26) that (27) represents a symmetric operator acting on u.
The corresponding operator in three dimensions is

$$\langle \nabla \tilde{w}, \nabla \tilde{u}_i \rangle_h \leftrightarrow ((B^z \otimes B^y \otimes A^x) - (L^{zT} \otimes L^{yT} \otimes L^{xT})(B^z \otimes B^y \otimes A^x))\tilde{u}_i + ((B^z \otimes A^y \otimes B^x) - (L^{zT} \otimes L^{yT} \otimes L^{xT})(B^z \otimes A^y \otimes B^x))\tilde{u}_i$$
$$+ ((A^z \otimes B^y \otimes B^x) - (L^{zT} \otimes L^{yT} \otimes L^{xT})(A^z \otimes B^y \otimes B^x))\tilde{u}_i, \tag{28}$$

for each velocity component $u_i, i = 1, 2, 3$.

Following the procedure for discretization of terms with spatially dependent coefficients described in [18], we can write

$$\langle \nabla \tilde{w}, 2v_T(x, y, z) \nabla \tilde{u}_i \rangle_h \leftrightarrow 2\,(I^z \otimes I^y \otimes D^{xT})V(I^z \otimes I^y \otimes D^x)\tilde{u}_i - 2\,(L^{zT} \otimes L^{yT} \otimes (D^xL^x)^T)V(I^z \otimes I^y \otimes D^x)\tilde{u}_i + 2\,(I^z \otimes D^{yT} \otimes I^x)$$
$$\times V(I^z \otimes D^y \otimes I^x)\tilde{u}_i - 2\,(L^{zT} \otimes (D^yL^y)^T \otimes L^{xT})V(I^z \otimes D^y \otimes I^x)\tilde{u}_i + 2\,(D^{zT} \otimes I^y \otimes I^x)V(D^z \otimes I^y \otimes I^x)\tilde{u}_i$$
$$- 2\,((D^zL^z)^T \otimes L^{yT} \otimes L^{xT})V(D^z \otimes I^y \otimes I^x)\tilde{u}_i. \tag{29}$$

In this equation, D denotes the GLL derivation matrix in each direction. Furthermore, the values of the eddy viscosity are lumped with the GLL integration weights in the diagonal matrix V with the entries $v_T^{rst}\rho_r^x\rho_s^y\rho_t^z$, in which rst are the grid point indices and V is ordered to be consistent with the ordering of the element grid points.

We are now finally ready to consider the model term in the form given in (11). Since the product of a symmetric and an anti-symmetric tensor is zero, we only need to compute the inner product

$$\langle \nabla \tilde{w}, 2v_T\nabla^s\tilde{\boldsymbol{u}} \rangle = \left\langle \frac{\partial \tilde{w}}{\partial x_j}, v_T\frac{\partial \tilde{u}_i}{\partial x_j} \right\rangle + \left\langle \frac{\partial \tilde{w}}{\partial x_j}, v_T\frac{\partial \tilde{u}_j}{\partial x_i} \right\rangle. \tag{30}$$

In tensor product form, the VMS small-scale dissipation term for the first component of the momentum equation becomes

$$\langle \nabla \tilde{w}, 2v_T(x, y, z)\nabla^s\tilde{u}_1 \rangle_h \leftrightarrow 2\,\{(I^z \otimes I^y \otimes D^{xT}) - (L^{zT} \otimes L^{yT} \otimes (D^xL^x)^T)\}V(I^z \otimes I^y \otimes D^x)\tilde{u}_1 + \{(I^z \otimes D^{yT} \otimes I^x)$$
$$- (L^{zT} \otimes (D^yL^y)^T \otimes L^{xT})\}V(I^z \otimes D^y \otimes I^x)\tilde{u}_1 + \{(D^{zT} \otimes I^y \otimes I^x) - ((D^zL^z)^T \otimes L^{yT} \otimes L^{xT})\}$$
$$\times V(D^z \otimes I^y \otimes I^x)\tilde{u}_1 + \{(I^z \otimes D^{yT} \otimes I^x) - (L^{zT} \otimes (D^yL^y)^T \otimes L^{xT})\}V(I^z \otimes I^y \otimes D^x)\tilde{u}_2$$
$$+ \{(D^{zT} \otimes I^y \otimes I^x) - ((D^zL^z)^T \otimes L^{yT} \otimes L^{xT})\}V(I^z \otimes I^y \otimes D^x)\tilde{u}_3 \tag{31}$$

and we obtain similar expressions for the other two components. The couplings between the velocity components, introduced by the second term of (30), are handled by including the cross terms in the explicit part of the time splitting, leaving the Helmholtz problem for the velocity components uncoupled.

As seen from (31), the calculation of the VMS LES model terms requires several additional operations. The increase in total computational work will vary with the size and complexity of the simulation. For the cases considered in this paper the increase is in the range 20–40%, with the smallest relative increase for the largest simulations. To put these numbers into perspective, we note that a conservative estimate of the computational complexity of the three-dimensional spectral element method is $O(K^3N^4)$, which gives a 70% increase in computational time by increasing the polynomial order ($N - 1$) from 6 to 7, and about the same by increasing the number of elements in each dimension (K) from 5 to 6.

3.5. Smagorinsky model

The eddy viscosity $v_T(\boldsymbol{x}, t)$ is chosen in [2] as a Smagorinsky-type function:

$$v_T = (C_S'\Delta')^2|\nabla^s\tilde{\boldsymbol{u}}|, \tag{32}$$

or alternatively

$$v_T = (C_S'\Delta')^2|\nabla^s\bar{\boldsymbol{u}}|. \tag{33}$$

The former was labeled "small-small" in [3], while the latter was labeled "large-small".

As the purpose of the model term is to approximate the effect of the unresolved scales on the small scales, it is argued in [2] that (32) is more consistent with the physical basis of the method, whereas (33) appears to be a computationally attractive alternative. The results in [3,4] show that good results are obtained with both methods. However, in terms of the spectral element implementation, the "large-small" form is not a computational simplification. A more attractive form is instead the "full-small" term, as proposed in Refs. [17,31],

$$v_T = (C_S'\Delta')^2|\nabla^s\boldsymbol{u}|, \tag{34}$$

in which the scale extraction operators are avoided completely.

The term $|\nabla^s\boldsymbol{u}|$ can be written out as

$$|\nabla^s\boldsymbol{u}| = \sqrt{\frac{1}{2}\sum_{i=1}^{3}\sum_{j=1}^{3}\left(\frac{\partial u_i}{\partial x_j} + \frac{\partial u_j}{\partial x_i}\right)^2}. \tag{35}$$

We discuss the choice of values for the parameters C_S' and Δ' in Section 4.3.

3.6. Related implementations

Among the previous implementations of the VMS LES method, the work of Munts et al. [8] is most closely related to the present method. In [8], a time-discontinuous Galerkin method with a modal basis of Jacobi polynomials $P^{1,1}$ is applied to the

compressible Navier–Stokes equations in conservation form, and a Smagorinsky term corresponding to the "small-small" formulation is used. The discretization is varied in the "hp"-style, meaning that both the size of the elements, h, and the polynomial order, p, can vary. The highest polynomial order used in the paper is 3, and the best results are found when the small scales are represented only by the highest order polynomials.

Collis [32] describes an implementation of VMS in a Discontinuous Galerkin method for the compressible Navier–Stokes equations. This method is similar to the present method in that it employs polynomial bases to span the solution space in each element, and in that scale partitioning is performed in the polynomial wavenumber space.

4. Computational results

4.1. Channel flow

Fully developed turbulent flow in a plane channel is the simplest case of an inhomogeneous turbulence field, and this configuration has therefore been extensively used to assess the performance of turbulence models. The fluid domain is bounded by two infinitely large parallel solid walls, and the flow is driven by a constant mean pressure gradient in the streamwise (x) direction. The boundary conditions are no-slip at the solid walls, and periodicity is imposed in the streamwise and spanwise (z) directions, respectively. The wall-normal direction is thus y, and the channel *half-height* is denoted h.

The instantaneous flow field is three-dimensional and time-dependent, but the ensemble averaged (mean) flow field is unidirectional and statistically steady. If we let $\langle\cdot\rangle$ denote the ensemble average, we therefore have $\mathbf{U} = \langle\mathbf{u}\rangle = (U(y), 0, 0)$. The constant pressure gradient that is forcing the flow is included as a source term, hence the mean pressure $P = \langle p\rangle = 0$.

The *friction velocity*, u_τ, is defined by

$$u_\tau^2 \equiv v \cdot \left.\frac{dU}{dy}\right|_{\text{wall}}, \tag{36}$$

and this is used in the definition of the frictional Reynolds number: $\text{Re}_\tau \equiv u_\tau h/v$. The friction velocity is related to the total frictional forces acting on the walls; the right-hand side of (36) is simply the ensemble averaged wall shear stress. Variables nondimensionalized in *wall units*, i.e. scaled by using kinematic viscosity v and friction velocity u_τ, are marked with the superscript +. The forcing pressure gradient is related to the Reynolds number by

$$-\left(\frac{dP}{dx}\right) = \frac{\rho u_{\tau 0}^2}{h} = \frac{\rho v^2}{h^3}\,\text{Re}_{\tau 0}^2. \tag{37}$$

Integrating the x-component of the ensemble averaged Navier–Stokes equations in the wall-normal direction yields

$$0 = -\rho^{-1}\left(\frac{dP}{dx}\right)y + v\frac{dU}{dy} - \langle u'v'\rangle. \tag{38}$$

Hence, in fully developed plane channel flow the sum of the viscous (vdU/dy) and turbulent ($-\langle u'v'\rangle$) stresses must vary linearly across the channel. This is a particularly useful analytical result that can be used a posteriori to assess the accuracy of the numerical solution. The turbulent shear stress contribution dominates across the channel except in a region very close to the wall where the viscous shear stress dominates, with $vdU/dy \to u_\tau^2$ as the wall is approached. This region is usually referred to as the viscous sub-layer, and its thickness decreases with increasing Reynolds number.

In shear generated turbulence, turbulence energy is extracted from the mean flow field by mean shear. Turbulent kinetic energy is subsequently dissipated into heat by the action of molecular viscosity. The latter process takes place at the smallest scales, and this physical process constitutes in essence the motivation for subgrid scale stress modelling in LES. Fully developed channel flow considered in this study constitutes a turbulent shear flow close to equilibrium, i.e. where the rate of production of turbulent kinetic energy is approximately balanced by the rate of viscous dissipation. This is true except very close to the wall where diffusive processes become important. In order to provide a measure of the performance of the VMS LES model it is therefore relevant to compare the level of turbulent kinetic energy integrated across the channel, i.e.

$$\int_0^{2h} k\,dy = \int_0^{2h} \frac{1}{2}(\langle u^2\rangle + \langle v^2\rangle + \langle w^2\rangle)\,dy = k_u + k_v + k_w, \tag{39}$$

with the corresponding mean kinetic energy, i.e.

$$\int_0^{2h} K\,dy = \int_0^{2h} \frac{1}{2}(U^2 + V^2 + W^2)\,dy = K_U + K_V + K_W. \tag{40}$$

We consider three different Reynolds numbers: $\text{Re}_\tau = 180, 550$, and 950, in order to assess the approach in not only low, but also moderate Reynolds number flows. The VMS LES computations are compared with spectral element simulations with the dynamic Smagorinsky model using the same resolution and with reference solutions obtained from direct numerical simulations. The computational domain of $8 \times 2 \times 4$ length units is used for all the simulations, even though the domain sizes varies for the reference solutions. To check the dependence on the domain size, we performed an additional simulation

with a larger domain for $Re_\tau = 550$ – the case with the largest difference in domain size between our simulations and the reference domain. The results of that test, presented in Section 4.5, show very little influence from this variation in domain size on the variables presented here.

4.2. Reference simulations

4.2.1. Direct numerical simulations

As a first step towards our goal, to implement and evaluate the variational multiscale LES method in a high order spectral element flow solver, we performed a DNS to validate the code. To this end, we considered channel flow at $Re_\tau = 180$, which corresponds to the well-known benchmark simulations reported by Kim et al. [36]. We performed the actual comparison of the results with the updated data set reported by Moser et al. [33] who used a fully spectral Fourier/Chebyshev method with $128 \times 129 \times 128$ grid points.

The simulation was carried out on a computational domain that approximately corresponds to the reference simulation [33,36], see Table 1 for details. Across the channel we used 16 non-uniformly distributed elements with 8 nodal points in each element. It was advised in [19] that the wall-normal point distribution should mimic the Gauss–Lobatto–Chebyshev (GLC) integration points. We used this as a starting point for the element distribution in the wall-normal direction, but to improve the resolution in the region $10 < y^+ < 20$, the GLC points $\{\xi_k\}_{k=0}^K$ were "stretched" towards the walls, using

$$\tilde{\xi}_k = \mathrm{sgn}(\xi_k) \cdot (1 - (1 - |\xi_k|)^{1.2}). \tag{41}$$

The standard GLL/GL points were used inside each element, without further mapping. In the streamwise and spanwise directions we used 16×16 uniformly distributed elements with 8×8 nodal points per element. Thus, the total number of nodal points amounts to $112 \times 113 \times 112$ in the streamwise, wall-normal, and spanwise directions, respectively. The solution was advanced in time with a time-step corresponding to 0.18 viscous time-units (v/u_τ^2), and with 50% polynomial filtering [25] on each time-step. The simulation was initiated by a flow field obtained from an existing plane channel flow solution obtained by a finite-volume code. The flow then evolved for approximately 54 flow-through times before a fully developed state was achieved. The results presented here were obtained by collecting statistics over approximately 20 flow-through times. The flow statistics are averaged both spatially over the homogeneous – streamwise (x) and spanwise (z) – directions, and in time. Homogeneity in a specific direction physically implies that statistical correlations comprising fluctuating quantities are spatially constant in that direction.

4.2.2. Under-resolved no-model simulations

As a precursor to the LES computations that are presented below, we also performed a coarser simulation, with $6 \times 6 \times 6$ elements, to assess the performance in a case that is spatially under-resolved. The element interfaces in the wall-normal direction were spaced according to a coarse Gauss–Lobatto–Chebyshev grid. In the streamwise and spanwise directions, we used a uniform element grid. In each element, we used $7 \times 7 \times 7$ nodal GLL points, giving a total resolution of $36 \times 37 \times 36$ nodal points. This mesh is referred to as Coarse-36 in Table 2. In this case we used 2% polynomial filtering to stabilize the simulation, and the same time-step as for the DNS. Otherwise, subgrid stresses were not explicitly accounted for. This computation can therefore either be interpreted as a "No-model" simulation or as a "Polynomial filtering-as-turbulence-model" simulation.

Table 1
Parameters for the present DNS and the reference simulations by Moser et al. [33] and by del Álamo et al. [34,35]. Grid spacing in wall units are calculated from the nominal Re_τ.

		Present DNS	Moser et al.	del Álamo & Jiménez	del Álamo et al.
	Nominal Re_τ	180	180	550	950
	Actual Re_τ	178.83	178.13	546.74	933.96
Domain dimensions	L_x	8	4π	8π	8π
	L_y	2	2	2	2
	L_z	4	$\frac{4}{3}\pi$	4π	3π
Total number of grid points	N_x	112	128	1536	3072
	N_y	113	129	257	385
	N_z	112	128	1536	2304
Grid spacing	Δx^+ mean	12.9	17.7	9.0	8.9
	Δy^+ min	0.10	0.054	0.041	0.032
	Δy^+ max	8.6	4.4	6.7	7.8
	Δz^+ mean	6.4	5.9	4.5	4.5
	Elements	16^3	–	–	–
	Pol. order ($N-1$)	7	–	–	–

4.2.3. Dynamic Smagorinsky simulations

We have also performed simulations with the dynamic Smagorinsky model [37] to obtain an additional point of reference for the VMS LES results presented below. Blackburn and Schmidt [38] discuss implementation of the dynamic model in spectral element discretizations.

We implemented the dynamic model using low-pass filtering in the Legendre polynomial basis as the test filter with the filter ratio $\Delta_{\text{test}}/\Delta = 2$, i.e. the test-filtered field comprises half of the modes of the resolved (filtered) field. The turbulent eddy viscosity is similar to the full-small term given in Eq. (34) with the exception that length scale $l^2 = (C_s\Delta)^2$ in this case is determined adaptively. To avoid negative values of the eddy viscosity that tend to de-stabilize the computations, we perform low-pass filtering in time of the estimated $(C_s\Delta)^2$ through the two-point recurrence [39]

$$(C_s\Delta)^{2(n+1)} = \epsilon(C_s\Delta)^{2(*)} + (1-\epsilon)(C_s\Delta)^{2(n)},$$

where $(C_s\Delta)^{2(*)}$ denotes the current estimate. This filtering eliminates most of the negative values; finally we use clipping of the remainder to ensure a non-negative eddy viscosity.

To validate the implementation of the dynamical model we performed simulations of the channel flow at $Re_\tau = 180$ using the same mesh (Coarse-36) and time-step as in the under-resolved simulation specified above. To stabilize the simulation we used over-integration and no polynomial filtering.

4.2.4. Results

We show the mean velocity and second order statistics in Figs. 6–9. Note that in these, and in all subsequent figures, the results are scaled against the nominal friction velocity $u_{\tau0}$. The resolved DNS results compare very well with the benchmark data, apart from a slight deviation in the buffer region ($20 < y^+ < 50$). In order to assess the accuracy more quantitatively the computed Reynolds number is compared to the imposed $Re_\tau = 180$. The actual computed Reynolds number is $Re_\tau = 178.8$, i.e. within 0.7% of the prescribed value. Moser et al. [33] reported $Re_\tau = 178.1$.

The turbulent-to-mean kinetic energy ratio displayed in Table 3 obtained in the present study, $k/K = 0.01394$, is close to the benchmark value of $(k/K)_{\text{Ref}} = 0.01378$, and the same goes for the turbulence anisotropies, $k_u/k, k_v/k$, and k_w/k.

It is believed that the accuracy of the present DNS could be even further improved by simply collecting statistics for a longer period of time. This was, however, not considered to be necessary. We conclude that the present results are in good correspondence with the benchmark data, thus establishing solid confidence in the numerical method.

The spatially under-resolved simulation give a computed Reynolds number $Re_\tau = 177.9$, i.e. within 1.2% of the prescribed value. The second order statistics for the velocity components and the kinetic energy measures also agree well with the reference, as we can see in Figs. 7, 8 and Table 3. This simulation can therefore be considered a "quasi-DNS", and this seems to indicate that the channel flow at $Re_\tau = 180$ is not a sufficiently challenging case for the assessment of turbulence models since the resolution required to obtain acceptable solutions is not severe. We have therefore used even coarser meshes in the VMS LES computations reported below. The most testing of the quantities plotted here is the fluctuating pressure, shown in Fig. 9, as the pressure is calculated from the Poisson-like Eq. (16b), with velocity gradients on the right-hand side. Any under-resolved simulation will yield significantly worse results in this case.

For each of the VMS LES test cases reported below, we also performed simulations without the VMS model, but with 2% polynomial filtering which was necessary to stabilize those calculations. The global measures for these calculations are given in Table 3.

The simulation with the dynamic Smagorinsky model on the Coarse-36 mesh give a computed Reynolds number $Re_\tau = 167.7$, and both the second order statistics and the kinetic energy measures agree well with the reference data. The

Table 2
Grid parameters for the coarse grid simulations. Grid spacing in wall units are calculated from the nominal Re_τ.

		Coarse-24[†,‡]	Coarse-36[‡]	Coarse-42[†,‡]	Coarse-60[†,‡]
	Nominal Re_τ	180	180	550	950
Domain dimensions	L_x	8	8	8	8
	L_y	2	2	2	2
	L_z	4	4	4	4
Total number of grid points	N_x	24	36	42	60
	N_y	25	37	43	61
	N_z	24	36	42	60
Grid spacing	Δx^+ mean	60.0	40.0	104.8	126.7
	Δy^+ min	4.5	2.0	4.6	3.9
	Δy^+ max	29.8	21.1	57.4	68.8
	Δz^+ mean	30.0	20.0	52.4	63.3
	Elements	4^3	6^3	7^3	10^3
	Pol. order $(N-1)$	6	6	6	6

‡ 'No-model' and dynamic Smagorinsky computations.
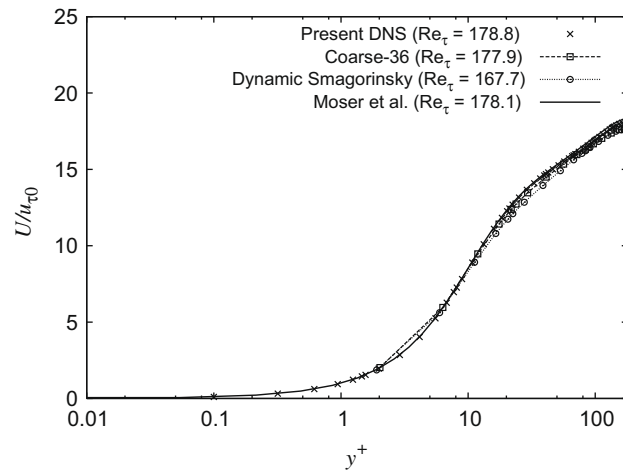† VMS LES computations.

Fig. 6. $Re_\tau = 180$: variation of the mean velocity across half the channel, compared with the reference solution of Moser et al. [33].
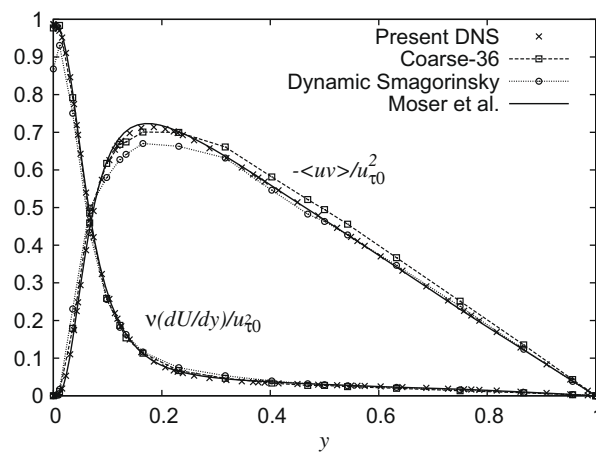

Fig. 7. $Re_\tau = 180$: variation of mean viscous shear and the turbulent shear stress across half the channel, compared with the reference solution of Moser et al. [33].
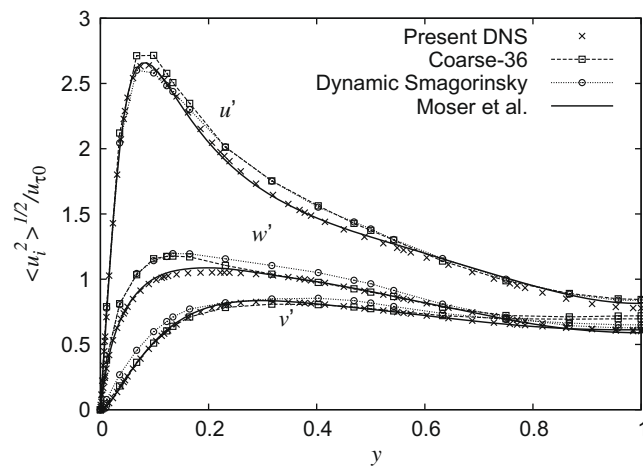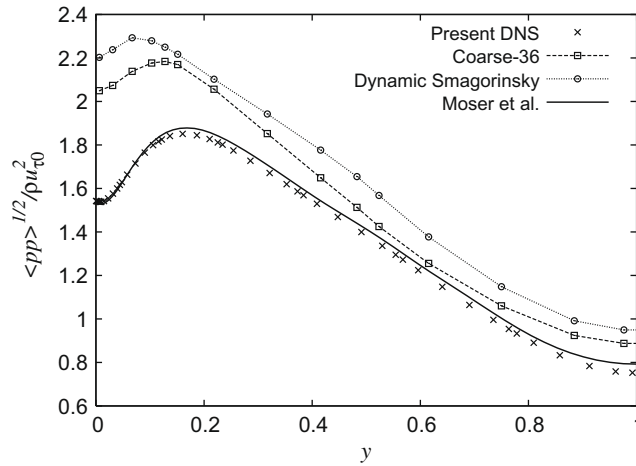

Fig. 8. $Re_\tau = 180$: variation of streamwise (u'), spanwise (v'), and wall-normal (w') root-mean-square velocity fluctuations across half the channel, compared with the reference solution of Moser et al. [33].

Fig. 9. $Re_\tau = 180$: variation of the root-mean-square pressure fluctuations across half the channel, compared with the reference solution of Moser et al. [33].

results also appear to agree well with results obtained with other implementations of the dynamic Smagorinsky model with comparable resolution – see for example [4,40] for simulations using global spectral methods.

4.3. VMS LES calculations

In order to test the performance of the VMS LES model, the computational grid was chosen significantly coarser than what would give reasonably good results without a subgrid scale model at all (see the previous section).

The main objective of this paper is to demonstrate a robust implementation of the VMS LES method. In order to assess the performace of the VMS method we will, for each case, present comparisons both with the reference DNS data and with the results from simulations with the dynamic Smagorinsky model using the same resolution. For other comparisons between VMS LES and other LES results in the framework of other discretization methods, we refer to e.g. [4,5,10,13,14,31,41,42,40].

The element interfaces in the wall-normal direction were given by a coarse Gauss–Lobatto–Chebyshev grid. The number of elements in the spectral element grids for the higher Reynolds numbers were chosen such that the first element interface in the wall-normal direction was placed at approximately the same value of y^+ for all the cases, see the illustrations in Fig. 5. This implies that the physical distance from the first element interface to the wall is reduced as the Reynolds number increases. To reduce the number of parameters, the polynomial degree was fixed for all the VMS LES runs; only the number of elements was changed. A summary of the grid parameters used for the various Reynolds numbers is presented in Table 2.

Table 3
Computed Re_τ, components of turbulent kinetic energy, and ratio of turbulent-to-mean kinetic energy (k/K) in plane channel simulations.

Case	Grid points	Re_τ	$\frac{1}{2}\langle u^2\rangle/k$	$\frac{1}{2}\langle v^2\rangle/k$	$\frac{1}{2}\langle w^2\rangle/k$	k/K
Nominal $Re_\tau = 180$						
Reference DNS [33]	$128 \times 129 \times 128$	178.1	0.6578	0.1348	0.2074	0.013780
SEM DNS	$112 \times 113 \times 112$	178.8	0.6579	0.1353	0.2069	0.013940
SEM VMS LES	$24 \times 25 \times 24$	189.6	0.6616	0.1302	0.2082	0.017187
SEM No model†	$24 \times 25 \times 24$	186.5	0.6738	0.1265	0.1997	0.022180
SEM Dynamic	$24 \times 25 \times 24$	158.9	0.6279	0.1361	0.2360	0.020650
SEM No model†	$36 \times 37 \times 36$	177.9	0.6577	0.1300	0.2123	0.015658
SEM Dynamic	$36 \times 37 \times 36$	167.7	0.6405	0.1385	0.2210	0.016224
Nominal $Re_\tau = 550$						
Reference DNS [34]	$1536 \times 257 \times 1536$	546.7	0.5604	0.1808	0.2589	0.010780
SEM VMS LES	$42 \times 43 \times 42$	552.6	0.5622	0.1860	0.2518	0.012423
SEM No model†	$42 \times 43 \times 42$	473.3	0.5091	0.2227	0.2682	0.025680
SEM Dynamic	$42 \times 43 \times 42$	428.7	0.4870	0.2346	0.2784	0.025710
Nominal $Re_\tau = 950$						
Reference DNS [35]	$3072 \times 385 \times 2304$	934.0	0.5580	0.1848	0.2571	0.009758
SEM VMS LES	$60 \times 61 \times 60$	884.2	0.5249	0.2104	0.2647	0.010755
SEM No model†	$60 \times 61 \times 60$	781.2	0.4739	0.2416	0.2845	0.022911
SEM Dynamic	$60 \times 61 \times 60$	739.1	0.4609	0.2496	0.2895	0.025581

† No-model simulations were stabilised by 2% polynomial filtering.

All the VMS LES results presented here were obtained using over-integration in order to achieve stable simulations on such coarse grids. The polynomial filtering [25], did actually reduce rather than improve the quality of the results when used in combination with the VMS LES model, and was therefore not used in these computations. An explanation for this can be that the transfer of energy between the highest order polynomials described in Section 3.1 interferes with the VMS LES model term and thus disturbs the model effect. The time-step was 0.0002 for all the coarse grid simulations.

The Smagorinsky model term given in Eqs. (32)–(34), contains two model parameters: The Smagorinsky constant, C_S', and the Smagorinsky length scale, Δ'. For plane channel flow, the traditional choice of the Smagorinsky constant is $C_S' = 0.1$ [43], and this value has also been used in the VMS calculations reported in Refs. [4,5]. We have also used this value. Note however that we performed a sensitivity test with respect to this parameter that is reported in Section 4.4. For the Smagorinsky length scale, we calculated Δ' for each element as the geometric average of the mean grid spacing in each direction. John and Roland [41] compared length scales based on the geometric average and the shortest edge of each element in a low order Finite Element VMS method. They found the results for the two formulations to be almost indistinguishable, whereas they had a large impact on the results of non-multiscale simulations using the Smagorinsky model with van Driest damping.

4.4. VMS LES results for $\mathrm{Re}_\tau = 180$

A number of combinations of the scale partitioning parameter, $\overline{N}$, and the various Smagorinsky forms were tested at $\mathrm{Re}_\tau = 180$, and the best choice was subsequently used for additional simulations at $\mathrm{Re}_\tau = 550$ and $\mathrm{Re}_\tau = 950$. The spectral element grid for $\mathrm{Re}_\tau = 180$ was chosen as the "Coarse-24" grid described in Table 2. The scale partitioning cut-off mode was the same for all elements, even though the element size varied in the wall-normal direction. Beside using different forms of the Smagorinsky term (32)–(34), the scale partitioning was varied as well in the simulations. With a local grid consisting of 7 grid points in each direction on each element, we used $\overline{N} = 4, \overline{N} = 5$, and $\overline{N} = 6$ for the large-scale extraction described in Section 3.2. These values correspond to approximately 57%, 71%, and 86%, respectively, of the one-dimensional Legendre polynomial spectrum. In three dimensions, the resulting large-scale spaces consist of approximately 19%, 35%, and 63% of the modes, respectively. Because of the relatively low polynomial order ($N = 7$) used in these simulations, varying $\overline{N}$ has quite large influence on the solution. The results shown in Figs. 10 and 11 suggest that $\overline{N} = 5$ constitutes the best choice in this case, so this is used for the remaining simulations for $\mathrm{Re}_\tau = 180$. To better study the sensitivity to $\overline{N}$, N should be at least 12, which would give "too good" results for the relatively simple case of $\mathrm{Re}_\tau = 180$. Therefore, a more detailed study of the sensitivity to the scale partitioning is done for $\mathrm{Re}_\tau = 550$ and discussed in Section 4.5.

The different forms of the Smagorinsky term gave similar results at the lowest $\mathrm{Re}_\tau = 180$, as can be seen in Figs. 12–14. The "large-small" Smagorinsky form (33) was employed at the two lowest Re_τ and the results were almost indistinguishable from the "full-small" (34) results. Results obtained with the former are therefore not included here.

The sensitivity to the chosen constant value of the Smagorinsky constant C_S' is tested by doubling and halving it. Results for the "full-small" Smagorinsky form are shown in Figs. 15 and 16. $C_S' = 0.2$ improves the mean velocity profile, while $C_S' = 0.05$ gives markedly worse results for the wall-normal and spanwise RMS velocity fluctuations – similar to the results without VMS model (not shown here). The conclusion of this simple sensitivity test is that $C_S' = 0.1$ is a reasonable choice, and smaller values should not be used.
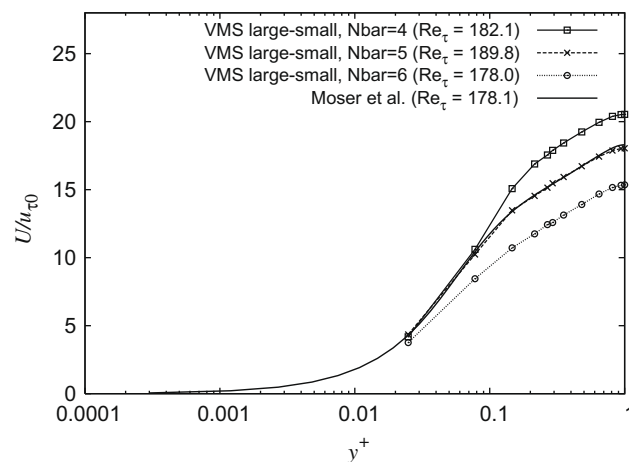

Fig. 10. $\mathrm{Re}_\tau = 180$: variation of the mean velocity across half the channel for different values of the scale partitioning parameter $\overline{N}$, compared with the reference solution of Moser et al. [33].
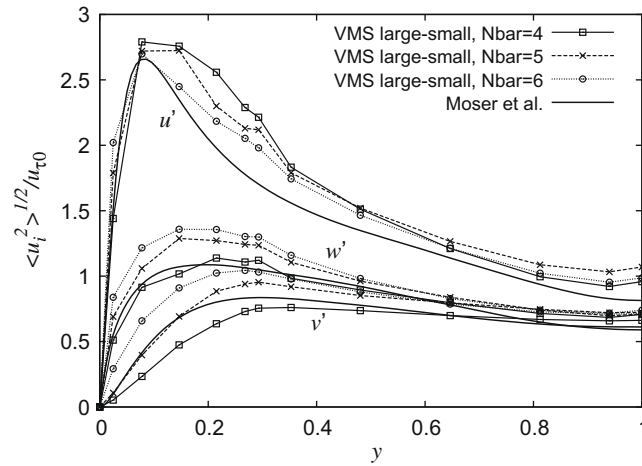
Fig. 11. $Re_\tau = 180$: variation of streamwise (u'), spanwise (w'), and wall-normal (v') root-mean-square velocity fluctuations across half the channel for different values of the scale partitioning parameter $\overline{N}$, compared with the reference solution of Moser et al. [33].
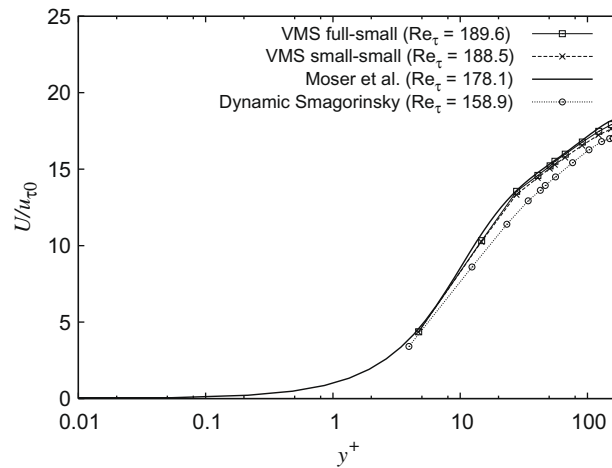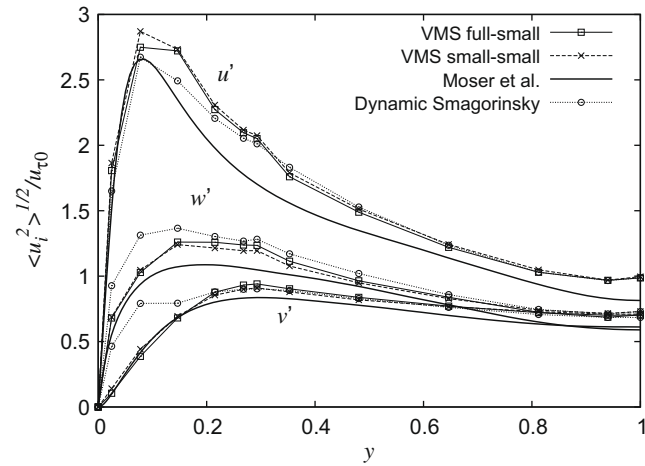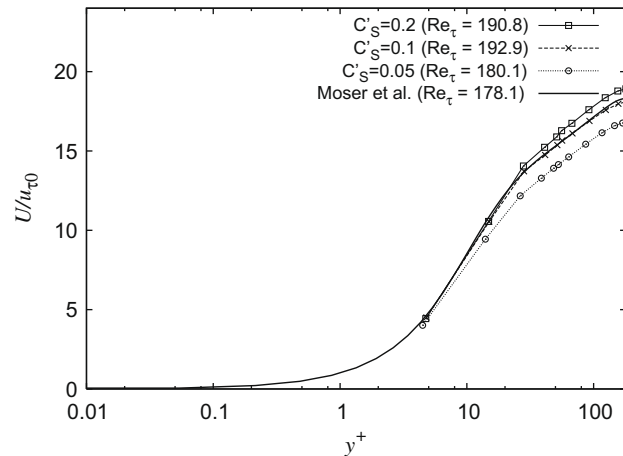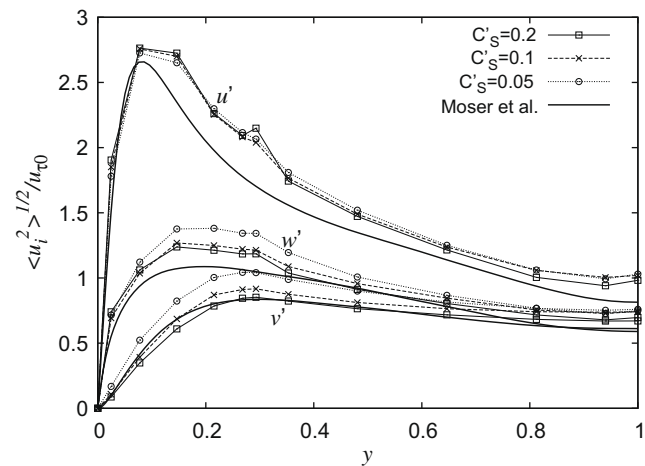

Fig. 12. $Re_\tau = 180$: variation of the mean velocity across half the channel for different forms of the Smagorinsky term, compared with spectral element dynamic Smagorinsky simulations performed with the same resolution and the reference solution of Moser et al. [33].
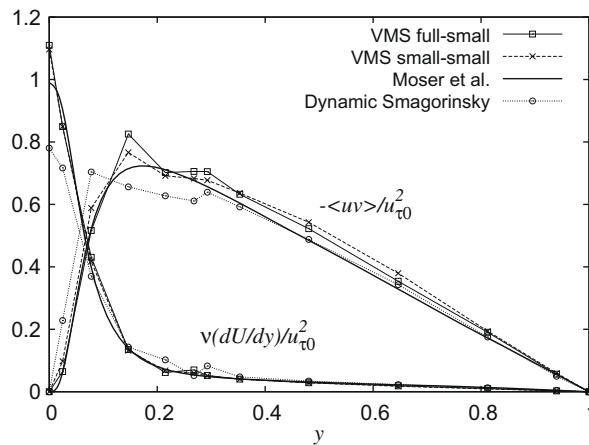
Fig. 13. $Re_\tau = 180$: variation of mean viscous shear and the turbulent shear stress across half the channel for different forms of the Smagorinsky term, compared with spectral element dynamic Smagorinsky simulations performed with the same resolution and the reference solution of Moser et al. [33].

Fig. 14. $Re_\tau = 180$: variation of streamwise (u'), spanwise (w'), and wall-normal (v') root-mean-square velocity fluctuations across half the channel for different forms of the Smagorinsky term, compared with spectral element dynamic Smagorinsky simulations performed with the same resolution and the reference solution of Moser et al. [33].

Fig. 15. $Re_\tau = 180$: variation of the mean velocity across half the channel for different forms of the Smagorinsky constant C'_S, compared with the reference solution of Moser et al. [33].

Fig. 16. $Re_\tau = 180$: variation of streamwise (u'), spanwise (w'), and wall-normal (v') root-mean-square velocity fluctuations across half the channel for different values of the Smagorinsky constant C'_S, compared with the reference solution of Moser et al. [33].

4.5. VMS LES results for $Re_\tau = 550$

The effect of the "full-small" and "small-small" becomes evident at $Re_\tau = 550$, where the former appears to perform better, see Figs. 17–19. These simulations are run on the "Coarse-42" grid described in Table 2. The mean velocity profile and the turbulent shear stress are captured well by the "full-small" model, whereas the turbulent kinetic energy is somewhat overpredicted (especially due to the overprediction of $\langle u^2 \rangle$). The "small-small" model predicts even higher turbulence levels which is reflected by a substantial underprediction of the mean velocity across the channel.

To study the effect of the scale partitioning parameter $\overline{N}$, a set of simulations with higher polynomial order was run. The grid used has 4 elements in each direction and $N = 12$ grid points in each direction. As for the other VMS LES grids, the element interfaces in the wall-normal direction are given by Gauss–Lobatto–Chebyshev grid points. The test in Section 4.4 showed that using 71% of the modes in the one-dimensional Legendre spectrum for the large-scale space worked better than 57% or 86%. In this test, with 12 polynomial modes, the variation between the results are smaller and the trends are easier to see. Figs. 20 and 21 show that the simulations with $\overline{N} = 8, 9$, and 10 give the best results, corresponding to 67%, 75%, and 83% of the modes, respectively. This is consistent with the previous test, and we can give a recommendation of using around three quarters of the modes in the one-dimensional Legendre spectrum for the large-scale space.

As mentioned in Section 4.3, the reference domain is larger than the present domain, and it should be investigated how this influences the results. For $Re_\tau = 550$, the difference in size is a factor π in the streamwise and spanwise directions. A simulation with doubled dimensions in these directions (to a $16 \times 2 \times 8$-domain) was also conducted, and results are shown
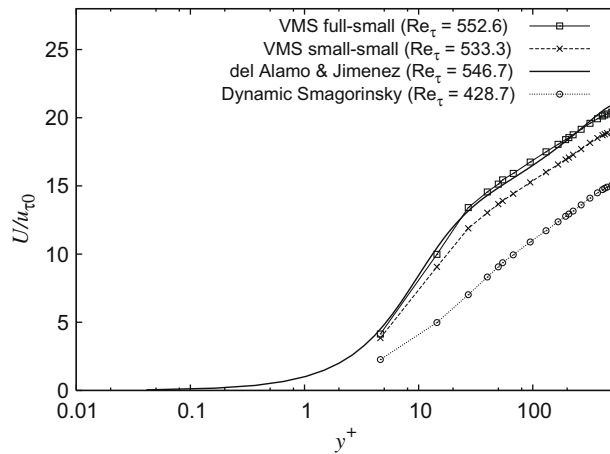

Fig. 17. $Re_\tau = 550$: variation of the mean velocity across half the channel for different forms of the Smagorinsky term, compared with spectral element dynamic Smagorinsky simulations performed at the same resolution and the reference solution of del Álamo and Jiménez [34].
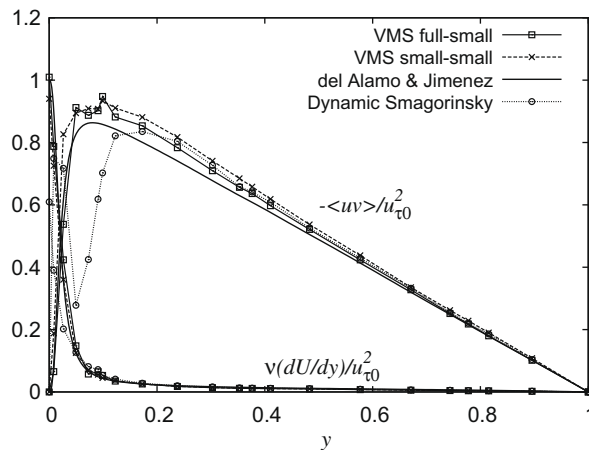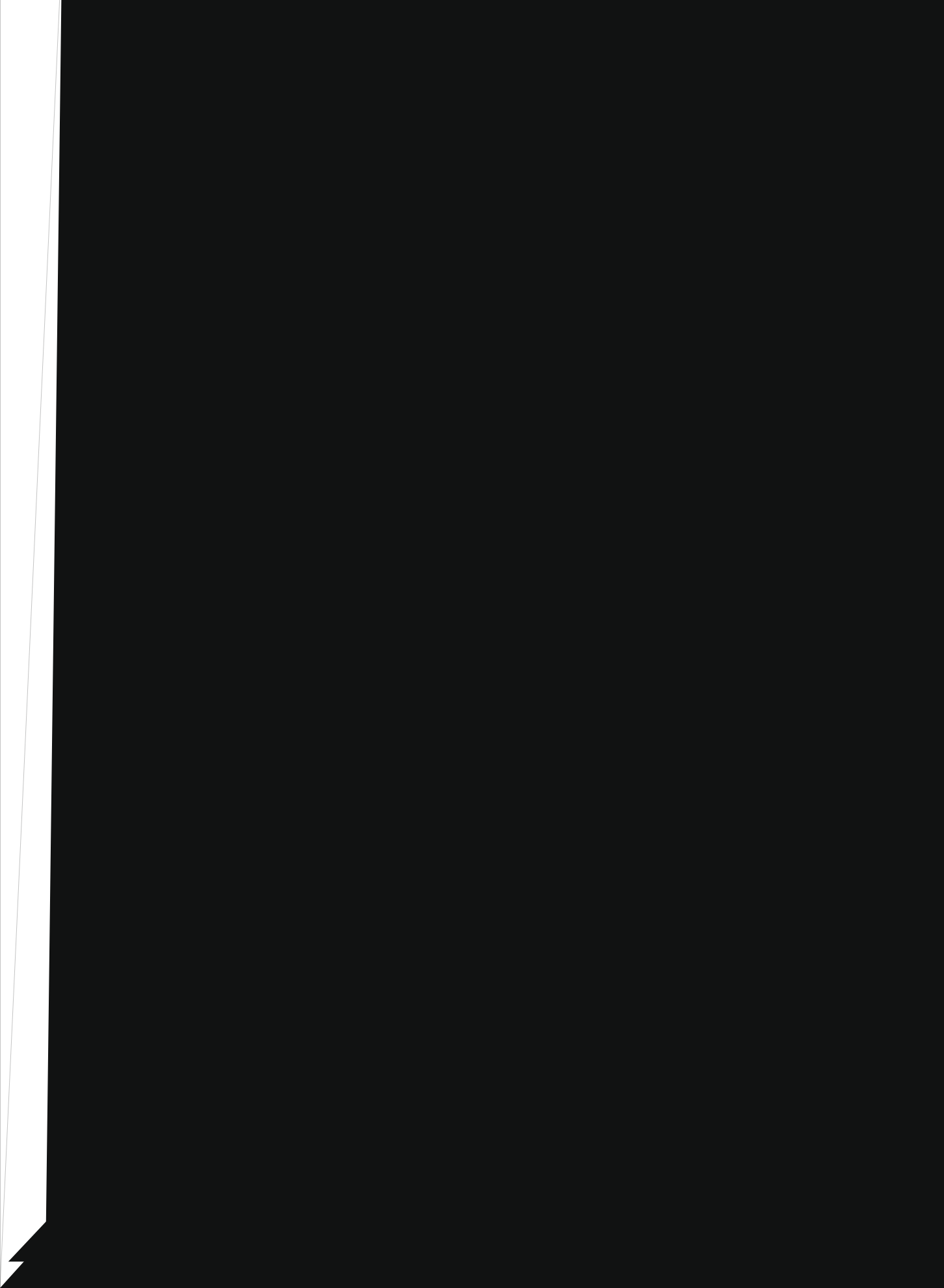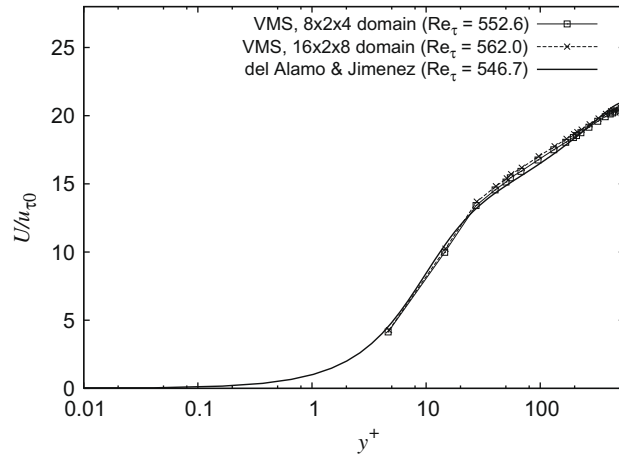

Fig. 18. $Re_\tau = 550$: variation of mean viscous shear and the turbulent shear stress across half the channel for different forms of the Smagorinsky term, compared with spectral element dynamic Smagorinsky simulations performed at the same resolution and the reference solution of del Álamo and Jiménez [34].

Fig. 22. $Re_\tau = 550$: variation of the mean velocity across half the channel for two computational domains of different size, compared with the reference solution of del Álamo and Jiménez [34].
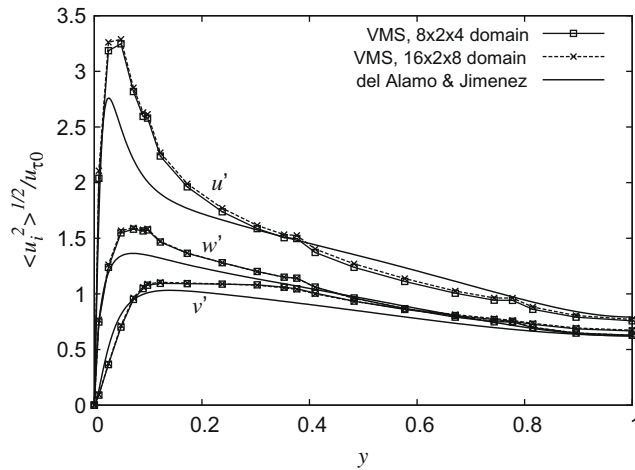

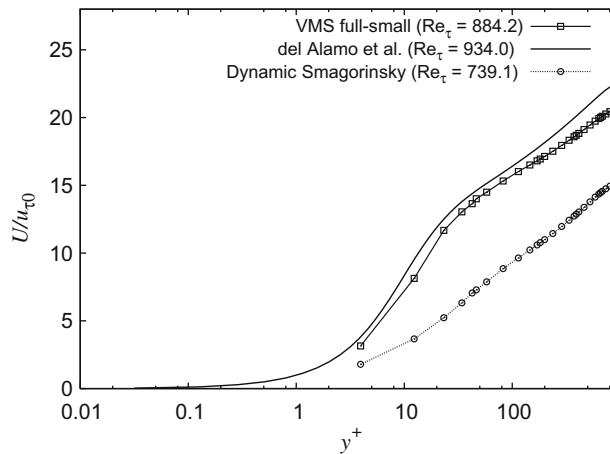**Fig. 23.** $Re_\tau = 550$: variation of streamwise (u'), spanwise (w'), and wall-normal (v') root-mean-square velocity fluctuations across half the channel for two computational domains of different size, compared with the reference solution of del Álamo and Jiménez [34].

Fig. 24. $Re_\tau = 950$: variation of the mean velocity across half the channel, compared with spectral element dynamic Smagorinsky simulations performed at the same resolution and the reference solution of del Álamo et al. [35].
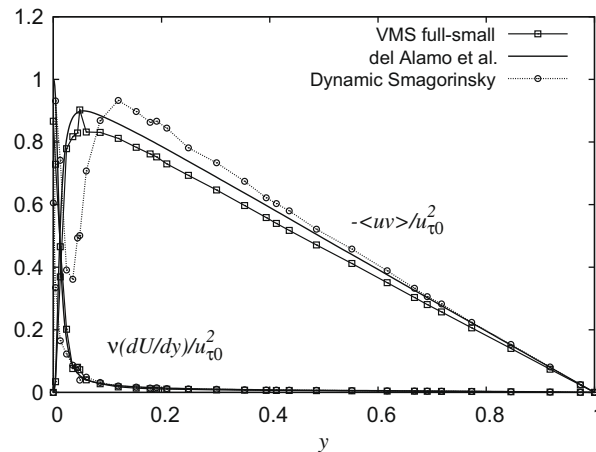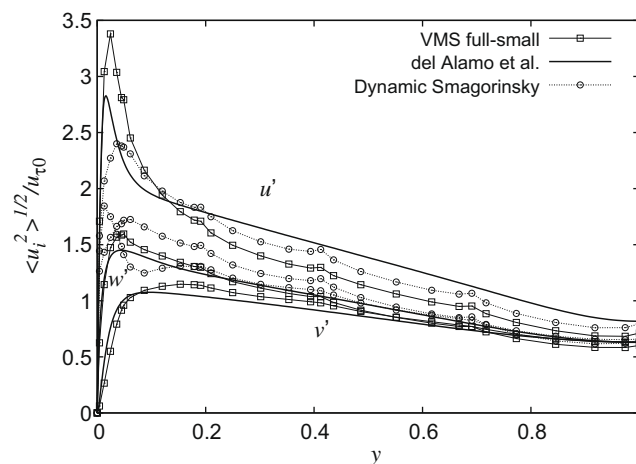
Fig. 25. $\mathrm{Re}_\tau = 950$: variation of mean viscous shear and the turbulent shear stress across half the channel, compared with spectral element dynamic Smagorinsky simulations performed at the same resolution and the reference solution of del Álamo et al. [35].

Fig. 26. $\mathrm{Re}_\tau = 950$: variation of streamwise (u'), spanwise (w'), and wall-normal (v') root-mean-square velocity fluctuations across half the channel, compared with the reference solution of del Álamo et al. [35].

in Figs. 22 and 23. The conclusion is that the doubling of the domain size in the streamwise and spanwise direction has practically no impact on the results presented here, so we assume that a further factor of $\pi/2$ to obtain the reference domain would not change the results significantly.

4.6. VMS LES results for $\mathrm{Re}_\tau = 950$

At $\mathrm{Re}_\tau = 950$ only the "full-small" Smagorinsky form was used, since this form appeared to perform better than the 'small-small' variant at $\mathrm{Re}_\tau = 550$ The grid was "Coarse-60" from Table 2. The present results compare relatively well with the reference data [35], although the turbulent shear stress, and thus also the turbulent kinetic energy, is somewhat over-predicted, see Figs. 24–26. These results suggest that the performance of the present VMS LES "full-small" model is rather robust.

The turbulent-to-mean kinetic energy ratio, k/K, integrated across the channel, exhibits a monotonic decrease with increased Reynolds number, both for the benchmark data and the VMS data, see Table 3. The model overpredicts in general the kinetic energy ratio, most severely at the lowest Reynolds number. These results suggest that the subgrid scale model is not dissipative enough.

5. Concluding remarks

The variational multiscale large eddy simulation method has been implemented within the framework of a spectral element method. The presented scale partitioning method was shown to produce a gradual introduction of the small-scale

model terms. It is documented that this is favourable to a sharp cut-off at a given point in the global spectral space [29,30]. The computational overhead for the method was 20–40% for the applications considered here. This must be considered to be acceptable, as even small increases in the spatial resolution of the spectral element method are more computationally demanding. Good results have been obtained – with the simplest possible small-scale dissipation model, and with grid densities as low as 0.06% of the reference simulation grid density – for fully developed plane channel flows up to $Re_\tau = 950$.

Simulations with the dynamic Smagorinsky model were also performed at the selected Reynolds numbers and resolutions. In all cases the dynamic model significantly underpredicts the computed wall friction. At $Re_\tau = 180$ the mean and RMS profiles computed with the dynamic model agree well with the reference data and the VMS solution. At the higher Re_τ, however, the VMS results appear to be in better agreement with the reference data than the results obtained with the dynamic model. For the cases considered here, the simulation time for the dynamic model is 10–20% longer than for the VMS model. The computational complexity of the two models are therefore largely comparable.

In closing, we observe that the traditional fully developed plane channel flow at $Re_\tau = 180$ does not seem to provide sufficient challenges for the testing of turbulence models, since the resolution requirement for a "quasi-DNS" at this very low Reynolds number is not severe.

Acknowledgements

References

[1] D. Carati, G. Winckelmans, H. Jeanmart, On the modelling of the subgrid-scale and filtered-scale stress tensors in large-eddy simulation, J. Fluid Mech. 441 (2001) 119–138.
[2] T.J.R. Hughes, L. Mazzei, K.E. Jansen, Large eddy simulation and the variational multiscale method, Comput. Visual. Sci. 3 (2000) 47–59.
[3] T.J.R. Hughes, L. Mazzei, A.A. Oberai, A.A. Wray, The multiscale formulation of large eddy simulation: Decay of homogeneous isotropic turbulence, Phys. Fluids 13 (2001) 505–512.
[4] T.J.R. Hughes, A.A. Oberai, L. Mazzei, Large eddy simulation of turbulent channel flow by the variational multiscale method, Phys. Fluids 13 (2001) 1784–1799.
[5] S. Ramakrishnan, S. Collis, Turbulence control simulation using the variational multiscale method, AIAA J. 42 (4) (2004) 745–753.
[6] V. Gravemeier, W.A. Wall, E. Ramm, A three-level finite element method for the instationary incompressible Navier–Stokes equations, Comput. Methods Appl. Mech. Engrg. 193 (2004) 1323–1366.
[7] V. John, S. Kaya, A finite element variational multiscale method for the Navier–Stokes equations, SIAM J. Sci. Comput. 26 (5) (2005) 1485–1503.
[8] E.A. Munts, S.J. Hulshoff, R. de Borst, A modal-based multiscale method for large eddy simulation, J. Comput. Phys. 224 (2007) 389–402.
[9] C. Farhat, I. Harari, U. Hetmaniuk, The discontinuous enrichment method for multiscale analysis, Comput. Methods Appl. Mech. Engrg. 192 (2003) 3195–3209.
[10] V. Gravemeier, Scale-separating operators for variational multiscale large eddy simulation of turbulent flows, J. Comput. Phys. 212 (2) (2006) 400–435.
[11] C. Farhat, A. Rajasekharan, B. Koobus, A dynamic variational multiscale method for large eddy simulations on unstructured meshes, Comput. Methods Appl. Mech. Engrg. 195 (13–16) (2006) 1667–1691.
[12] S.S. Collis, Monitoring unresolved scales in multiscale turbulence modeling, Phys. Fluids 13 (2001) 1800–1806.
[13] H. Jeanmart, G.S. Winckelmans, Comparison of recent dynamic subgrid-scale models in turbulent channel flow, in: Proceedings of the Summer Program 2002, Center for Turbulence Research, NASA Ames/Stanford Univ., 2002, pp. 105–116.
[14] H. Jeanmart, G. Winckelmans, Investigation of eddy-viscosity models modified using discrete filters: A simplified regularized variational multiscale model and an enhanced field model, Phys. Fluids 19 (055110) (2007) 1–16.
[15] E. Tadmor, Convergence of spectral methods for nonlinear conservation laws, SIAM J. Numer. Anal. 26 (1989) 30–44.
[16] C. Xu, R. Pasquetti, Stabilized spectral element computations of high Reynolds number incompressible flows, J. Comput. Phys. 196 (2004) 680–704.
[17] A.W. Vreman, The filtering analog of the variational multiscale method in large-eddy simulation, Phys. Fluids 15 (8) (2003) L61–L64.
[18] M.O. Deville, P.F. Fischer, E.H. Mund, High-Order Methods for Incompressible Fluid Flow, Cambridge University Press, 2002.
[19] G.E. Karniadakis, S.J. Sherwin, Spectral/hp Element Methods for Computational Fluid Dynamics, Oxford University Press, 2005.
[20] Y. Maday, A. Patera, E.M. Rønquist, An operator-integration-factor method for time-dependent problems: Application to incompressible fluid flow, J. Sci. Comput. 4 (1990) 263–292.
[21] A.T. Patera, A spectral element method for fluid dynamics: Laminar flow in a channel expansion, J. Comput. Phys. 54 (1984) 468–488.
[22] Y. Maday, A.T. Patera, Spectral element methods for the incompressible Navier–Stokes equations, in: A.K. Noor (Ed.), State of the Art Surveys in Computational Mechanics, ASME, New York, 1989, pp. 71–143.
[23] C. Canuto, M.Y. Hussaini, A. Quarteroni, T.A. Zang, Spectral Methods in Fluid Dynamics, Springer-Verlag, 1988.
[24] R.M. Kirby, G.E. Karniadakis, De-aliasing on non-uniform grids: Algorithms and applications, J. Comput. Phys. 191 (2003) 249–264.
[25] P.F. Fischer, J.S. Mullen, Filter-based stabilization of spectral element methods, Comptes Rendus de l'Académie des sciences Paris, t.332, Série I – Analyse numérique (2001) 265–270.
[26] R. Pasquetti, C.J. Xu, Comments on filter-based stabilization of spectral element methods, J. Comput. Phys. 182 (2002) 646–650.
[27] P.F. Fischer, N.I. Miller, H.M. Tufo, An overlapping Schwarz method for spectral element simulation of three-dimensional incompressible flows, in: P. Bjørstad, M. Luskin (Eds.), Parallel Solution of Partial Differential Equations, Springer-Verlag, 2000, pp. 159–180.
[28] D. Gottlieb, S.A. Orszag, Numerical Analysis of Spectral Methods: Theory and Applications, SIAM, Philadelphia, 1977.
[29] P. Sagaut, V. Levasseur, Sensitivity of spectral variational multiscale methods for large-eddy simulation of isotropic turbulence, Phys. Fluids 17 (3) (2005) 035113.
[30] J. Meyers, P. Sagaut, On the model coefficients for the standard and the variational multi-scale Smagorinsky model, J. Fluid Mech. 569 (2006) 287–319.

[31] J. Holmen, T. Hughes, A. Oberai, G. Wells, Sensitivity of the scale partition for variational multiscale large-eddy simulation of channel flow, Phys. Fluids 16 (3) (2004) 824–827.
[32] S.S. Collis, The DG/VMS method for unified turbulence simulation, AIAA paper 2002-3124 (2002).
[33] R.D. Moser, J. Kim, N.N. Mansour, Direct numerical simulation of turbulent channel flow up to $Re_\tau = 590$, Phys. Fluids 11 (1999) 943–945.
[34] J.C. del Álamo, J. Jiménez, Spectra of the very large anisotropic scales in turbulent channels, Phys. Fluids 15 (6) (2003) L41–L44.
[35] J.C. del Álamo, J. Jiménez, P. Zandonade, R.D. Moser, Scaling of the energy spectra of turbulent channels, J. Fluid Mech. 500 (2004) 134–144.
[36] J. Kim, P. Moin, R. Moser, Turbulence statistics in fully developed channel flow at low Reynolds number, J. Fluid Mech. 177 (1987) 133–166.
[37] M. Germano, U. Piomelli, P. Moin, W. Cabot, A Dynamic subgrid-scale eddy viscosity model, Phys. Fluids A 3 (7) (1991) 1760–1765.
[38] H. Blackburn, S. Schmidt, Spectral element filtering techniques for large eddy simulation with dynamic estimation, J. Comput. Phys. 186 (2) (2003) 610–629.
[39] M. Breuer, Large eddy simulation of the subcritical flow past a circular cylinder: Numerical and modeling aspects, Int. J. Numer. Meth. Fluids 28 (9) (1998) 1281–1302.
[40] S. Stolz, P. Schlatter, L. Kleiser, High-pass filtered eddy-viscosity models for large-eddy simulations of transitional and turbulent flow, Phys. Fluids 17 (6) (2005) 065103.
[41] V. John, M. Roland, Simulations of the turbulent channel flow at Re-tau = 180 with projection-based finite element variational multiscale methods, Int. J. Numer. Methods Fluids 55 (5) (2007) 407–429.
[42] T. Iliescu, P. Fischer, Large eddy simulation of turbulent channel flows by the rational large eddy simulation model, Phys. Fluids 15 (10) (2003) 3036–3047.
[43] J. Deardorff, A numerical study of 3 dimensional turbulent channel flow at large Reynolds numbers, J. Fluid Mech. 41 (1970) 453–480.